

Magnetic Fields in Cluster Cores: Faraday Rotation in A400 and A2634

Jean A. Eilek

*Physics Department, New Mexico Tech
Socorro NM 87801*

and

Frazer N. Owen

*National Radio Astronomy Observatory¹,
Socorro, New Mexico 87801*

ABSTRACT

We present Faraday rotation data for radio sources in the centers of the Abell clusters A400 and A2634. These clusters contain large ($\gtrsim 100$ kpc), tailed radio sources, each attached to the central cD galaxy. These clusters do not have strong cooling cores. Our data extend previous work on rotation measure in cluster centers to larger scales and non-cooling clusters. The rotation measure, and thus the magnetic field, is ordered on scales $\sim 10 - 20$ kpc in both clusters. The geometry of the rotation measure appears to be determined by the distribution of the X-ray emitting gas, rather than by the radio tails themselves. We combine our data with previously published X-ray and radio data in order to analyze the magnetic fields in all 12 clusters whose central radio sources have been imaged in rotation measure. We find that the fields are dynamically significant in most clusters. We argue that the Faraday data measure fields in the intracluster medium, rather than in a skin of the radio source. Finally, we consider the nature and maintenance of the magnetic fields in these clusters, and conclude that either the cluster-wide field exists at similar levels, or that a weaker cluster-wide field is amplified by effects in the core.

Subject headings: galaxies: clusters – galaxies: magnetic fields – magnetic fields

¹The National Radio Astronomy Observatory is operated by Associated Universities, Inc., under a cooperative agreement with the National Science Foundation.

1. Introduction

The physical state of the plasma in clusters of galaxies is far from understood. One important question is whether that plasma is magnetized, and if so at what levels. Some important steps toward answering this question have already been made.

There is some evidence that modest fields exist throughout the intracluster medium (ICM). One approach uses the integrated rotation measure (RM) of sources in or behind clusters. Hennessy *et al.* (1989) compared sources seen through cluster cores to a non-cluster control sample, and found no significant excess RM in the cluster sample. In a similar study, Kim *et al.* (1991) did find excess RM in sources in and behind clusters (although the effect was less strong when they excluded radio sources embedded in the clusters). Clarke, Kronberg & Böhringer (2001; CKB) carried out a similar study with a more uniform sample, also using both background and cluster-member sources. They also find evidence for an intrinsic cluster field. The excess RM values suggested by the Kim *et al.* and the CKB work are consistent with modest magnetic fields, at a few μG levels, throughout the cluster. This work is not yet conclusive, however. Unresolved data can underestimate the true RM of a particular source. In addition, neither the Kim *et al.* nor the CKB work can distinguish between a few μG field intrinsic to the cluster, and a much weaker field which is enhanced only around the observed radio galaxies.

Another approach relies on the diffuse synchrotron radio haloes have been detected in several clusters (*e.g.*, Feretti & Giovannini 1996). Ongoing work (*e.g.*, Owen, Morrison & Voges 1999, Feretti 1999) suggests these are not as rare as has been thought. The simplest minimum-pressure or equipartition analyses find the field associated with these haloes is $\sim 0.1 - 1\mu\text{G}$. X-ray spectra from these halo clusters also allow the possibility of detecting microwave background photons which have been inverse Compton scattered up to the X-ray range. A non-detection in the X-rays leads to a lower limit to the magnetic field, generally in the sub-microgauss range (*e.g.*, Henriksen, 1998). Reported detections, if confirmed, also suggest similar field values (*e.g.*, Fusco-Femiano *et al.* 1999).

Thus, both the RM data and the radio halo data suggest magnetic fields in the $\sim \mu\text{G}$ range, throughout the volume of the cluster. These analyses have been carried out assuming a uniform, volume-filling magnetic field. We note that the data are also consistent with higher fields if the filling factor is small (which we argue below is likely to be the case).

Additional information comes from resolved RM images of radio sources within the cluster. Sources in cluster center are easiest to interpret in terms of the associated magnetic field, due to the certainty of their position within the ICM. The best-studied clusters so far are those with strong central X-ray peaks, associated with cooler gas. These are the

clusters that have been interpreted as “cooling flows”. Several high-quality images exist for the RM associated with radio sources in the centers of such clusters (*e.g.*, Ge & Owen 1994; Taylor, Allen & Fabian 1999; and references therein). These authors find high RM values, several thousand rad/m², with order scales $\sim 1 - 10$ kpc are typical of radio sources in this environment.

Thus, present evidence supports a modest magnetic field, at microgauss levels, throughout most clusters. In addition, a much stronger field exists in the inner region of strong cooling cores. The connection between these two results is not yet clear. In this paper we extend the data base by presenting RM images of two larger, tailed radio galaxies in clusters which do not have strong cooling cores. We consider 3C75 in Abell 400, and 3C465 in Abell 2634. Both of these clusters have only weak central cooling. Both of the radio sources extend to $\gtrsim 100$ kpc, so that we can study a more significant fraction of the cluster core. We find the RM is ordered, on scales $\sim 10 - 20$ kpc, and that the order seems to depend more on the geometry of the X-ray gas than of the radio tails themselves. By combining this with gas densities determined from X-ray deprojection, we find the magnetic fields are likely to be dynamically important in these two clusters.

We begin by introducing the two clusters and presenting our new data (in §2). After reviewing basic assumptions necessary for RM analysis (in §3), in §4 we place our results in the context of all nearby clusters for which high-quality RM data of the central source is available. In §5 we consider possible mechanisms by which the magnetic field can be maintained. We present our conclusions in §6.

2. The Data: X-Ray Analysis and Rotation Measure Imaging

2.1. Abell 400

Abell 400 is a richness class 1, Rood-Sastry I cluster. Its dynamics have been analyzed by Beers *et al.* (1992). They find a mean redshift $z = .0235$, which corresponds to 26.5 kpc/amin, using $H_o = 75$ km/s-Mpc. After separating out a background group of galaxies to the NE, they find that the cluster itself has substructure. The central, elliptical-rich population is composed of two subgroups, separated by ~ 700 km/s. These groups are not apparent in the galaxy distribution projected on the sky. From this, they conclude that a merger is taking place, close to the line of sight. The cluster centers on a dominant galaxy with two nuclei separated by 435 km/s (*e.g.*, Balcells *et al.* 1995). The double nuclei have been interpreted as due to projection (Tonry 1985), as closely interacting (Lauer 1988) and as merging clump centers (Beers *et al.*, also Balcells *et al.*).

The X-ray image is fairly smooth, with some elongation of the inner isophotes (see also Beers *et al.* 1992 who present ellipse fits to the inner isophotes). Figure 1 shows the image from the ROSAT PSPC, together with the central radio galaxy. Abell 400 does not have a strong cooling core. White *et al.* (1997) agree with earlier authors in finding that any spherical mass inflow is small, $\dot{M} \lesssim 10M_{\odot}/\text{yr}$.

The central galaxy is host to an unusual radio source: each nucleus gives rise to a radio jet, and the jets merge into the striking tailed radio source, 3C75 (Owen *et al.* 1985). Figure 1 shows that the tails can be detected to ~ 7 amin ~ 185 kpc at 327 MHz. They bend to the NE, away from the X-ray centroid and axis of elongation. Note that our RM data (based on higher frequencies than the image in Figure 1) extend only to ~ 200 asec ~ 90 kpc.

2.2. Abell 2634

Abell 2634 is a richness class 1, Rood-Sastry cD cluster. It has a mean $z = .0313$ (Pinkney *et al.* 1993), which corresponds to 35.2 kpc/amin. Its dynamics and structure have been studied by Pinkney *et al.* and by Scoggio *et al.* (1995). While the dynamical situation is not totally clear, both papers agree on the most likely picture. The cluster itself does not show any evidence for substructure, either in velocity or physical space. The cluster sits in a complex area of the sky which also contains the lower redshift Pisces-Perseus supercluster. Two groups of galaxies sit $\sim 1^{\circ}$ to the east, one high-velocity and low-velocity relative to A2634. When these groups are excluded, the velocity and spatial structure of A2634 are consistent with a relaxed cluster. Thus based on the velocity field there is no evidence that A2634 is currently undergoing a major merger.

The X-ray image of this cluster is more complex than the optical data would suggest. On large scales, the isophotes are more or less regular; but on small scales a striking central elongation appears. Figure 2 shows the image from the ROSAT PSPC, together with the central radio galaxy (Eilek *et al.* 1984; also *c.f.* Schindler & Prieto 1996 who present inner X-ray isophotes). The distorted central X-ray distribution has no counterpart in the optical image. Although Schindler & Prieto (1996) argue against this distortion being caused by a merger, Roettiger, Loken & Burns (1997) find that such structures can indeed occur in the later stages of a merger. They find density elongations and bulk flows along the merger axis. As with Abell 400, there is no significant evidence of a cooling core in A2634 (White *et al.* 1997, who agree with earlier work).

The central galaxy also has a double nucleus (Lauer 1988). One of the nuclei gives rise to a large tailed radio galaxy, 3C465 (Eilek *et al.* 1984). The radio tails can be detected to

~ 7 amin ~ 250 kpc at 327 MHz. They bend to the SW, towards (and around) the X-ray elongation. Our RM map, again based on high frequencies, covers only the inner region, extending to ~ 230 asec ~ 135 kpc.

2.3. X-ray Analysis

The two clusters were observed in pointed observations with the ROSAT PSPC. We carried out a simple deprojection analysis to determine the density and temperature of the inner regions of each cluster. As the inner part of each cluster is distorted from circular symmetry, we allowed for this in our deprojection. (Beers *et al.* 1992 present ellipse fits to the surface brightness for A400, as do Schindler & Prieto 1996 for A2634. These papers display the elongated isophotes for each cluster, which can also be seen in Figures 1 and 2.) We used IRAF to fit elliptical contours to the surface brightness of each cluster, and to determine the flux from each elliptical annulus. The effective scale of the ellipse is \sqrt{ab} , if a and b are the semi-major and semi-minor axes. In order to determine the emitting volume of a particular ellipse, we assumed the major axis of each ellipse lies in the plane of the sky, and that the volumes were prolate ellipses. We then used an “onion-skin” method to deproject the data, as follows. At a given point on the sky, say some effective distance R from the X-ray peak, the surface brightness is a linear sum of the contributions from all elliptical shells lying at or outside R . If the number of shells is finite, as is the case with discretely sampled data, then the surface brightness can be deprojected using simple linear analysis to determine the intensity in each elliptical volume. (Fabian *et al.* 1981 describe a similar method, however assuming spherical symmetry).

We separated the X-ray data into the four R4 to R7 bands covering 0.5 to 2.05 keV within the ROSAT window (Snowden *et al* 1994), and carried out our analysis separately on each band. This gave us a four-point spectrum for each shell. Using XSPEC to estimate the emissivity as a function of temperature in each band, while holding metallicity constant at 0.3 solar which is typical of similar clusters (e.g. Edge & Stewart 1991), we fit both temperature and density in each shell.

Table 1 shows the density and temperature we derive for each elliptical shell. The density values are consistent with other analyses of non-cooling clusters such as these, and also with the analysis of Eilek & Markovic (2001). They find the size of the “gas core” (at which the density drops to 20% of its central value) to be ~ 300 kpc for A400, ~ 400 kpc for A2634. The temperature structure from Table 1 is worth comment. We find that both clusters have cooler gas in the inner $\sim 25 - 20$ kpc, outside of which the temperature rises to a warmer value which describes the cluster as a whole. Schindler & Prieto find a

similar result for the core of A2634; we are not aware of any spectral analysis for the core of A400. Our results for the large-scale temperatures are a bit lower than other authors find. White *et al.* (1997) find 2.1 keV for A400 and 3.4 keV for A2634 (full clusters), while Fukazawa *et al.* (1998) find 2.3 keV in A400, and 3.7 keV in A2634, for the region outside of 100 kpc. The reason for this discrepancy is not clear; we suspect that our use of elliptical isophotes combines cool and hot gas in a different way than the circular rings used by other authors. In addition, the poor temperature sensitivity of ROSAT to high-temperature gas may contribute to the discrepancy.

For the purposes of this paper, we use this analysis to extract typical densities and pressures characteristic for the region in which we have Faraday rotation data, namely, the inner 100 - 200 kpc of each cluster. This will be used in §4, below.

2.4. Rotation Measure Imaging

VLA observations were carried out using the C and D arrays in four frequency bands each within the C-band (4.5-5.0 GHz) and the X-band (8.0-8.9 GHz) for a total of eight frequencies. Standard calibration, including instrumental polarization, was applied to the data. After cleaning and imaging using AIPS, we determined the rotation measures using a modified version of the AIPS task, RM, which took all eight frequencies as input. The RM program also produces an estimate of the intrinsic magnetic field direction by correcting the polarization vectors to zero wavelength from the rotation measure and adding 90 degrees.

We thus determined the rotation measure, and also the intrinsic direction of the magnetic field, projected on the plane of the sky. In Figures 3 and 4 we show the projected magnetic field directions for each source. We see that the two sources have different characteristics in projected field directions. 3C465, in A2634, has a projected field which more or less follows the radio tails. This is consistent with other sources in which the magnetic field agrees with the apparent flow direction. However, 3C75 in A400 is more complex; interesting small-scale loops and other field structures are apparent in Figure 3. We suspect this is due to the more complex flow field of this source (recalling that the total intensity image, Owen *et al.* 1985, shows loops and twists which suggest the two jets are interacting strongly). As our goal in this paper is the RM information, we defer analysis of the polarization in these two sources to a later paper.

We present the RM data in several ways. In Figures 5 and 6 we present RM images for each object, with the colors chosen to highlight positive and negative RM values. Alternating positive and negative RM patches are apparent in each source; the RM in each case appears

to have a characteristic “order scale” of 10 -20 kpc. These patches are well resolved; our restored beam was 3x3 asec (~ 1.3 kpc for 3C75, ~ 2.2 kpc for 3C465). We can characterize the RM distribution in terms of a mean and an rms. For A400, the mean is -7.6 rad/m², with rms 100 rad/m². For A2634, the mean is -25 rad/m², and the rms is 120 rad/m². The non-zero means could be due to galactic foreground, they could be a small mean RM due to the cluster itself, or they could simply be statistical fluctuations either in RM’s of the distant radio sources or structure in the galactic RM distribution. We cannot distinguish between these options, but this is not critical for our analysis here.

Structure in the RM can be studied with other displays. In Figures 7 and 8, we show the absolute value of the RM as a function of distance from the galactic core. These data are means within circular apertures, centered on the galactic core; the horizontal axis is the radius of each ring. The mean magnitude of the RM is approximately constant over ~ 50 kpc in A400, and drops by a factor ~ 2 over 80 kpc in A2634. We also find small patches of large RM magnitudes. Figures 9 and 10, we present color images of the absolute value of the RM for each source; the scaling is chosen to highlight the small patches of extreme $|RM|$ in the east tail of 3C465, and the west tail of 3C75.

2.4.1. *Rotation Measure Structure in Each Cluster*

These data show that the overall properties of the RM distribution in each cluster are quite similar. The images give a strong impression of order in the RM, rather than being purely random. Each source shows both positive and negative RM patches, with comparable areas showing positive and negative values. The projected scale of the patches is $\sim 10 - 20$ kpc in each object. What can we infer about the three-dimensional structure, or the physical location, of the field causing the RM, in each object? In A400, one’s first impression is of a set of positive and negative patches, without particular order. On closer inspection, however, the two highly negative patches ($RM \sim -250$ to -300 rad/m²) on the west tail stand out. In addition, two strongly positive patches ($RM \sim 150$ to 200 rad/m²) can be seen in the east tail. None of these areas correlate with any particular feature in the radio tails. It is tempting to interpret the two positive areas and two negative areas as being continuous bands of extreme RM, which happen to be projected on the radio tails. With this interpretation, it is interesting to note that the bands lie roughly parallel to the major axis of the X-ray elongation (as shown in Figure 1).

In A2634, order in the RM image is more striking. Clear positive and negative RM bands alternate along each tail. However, the relation of the RM to the tail geometry is different for the two tails. Along the west tail, the RM bands tend to lie across the tail;

along the east tail they tend to lie along it. The extreme RM values here are found in the east tail. The radio hot spot shows strongly positive and negative values, $\sim \pm 200$ rad/m², alternating across the hot spot. This is the one place in the two sources where extreme RM features appear to correlate with particular radio features. The RM bands just below this feature also have extreme RM values, in about the same range. However, they do not correlate with any particular radio feature. Once again, it is possible to interpret the data as continuous positive and negative RM features, which happen to be projected onto the radio tails. In this case, however, the RM bands lie roughly perpendicular to the major axis of the X-ray elongation (as shown in Figure 2).

2.4.2. *Location of the Faraday Screen*

The observed rotation measure is almost certainly due to an intervening magnetized plasma, rather than the radio source itself. This can be seen from two lines of argument.

First, consider the alternative case, in which the RM arises from the radio source itself. We can refer to Burn (1966), also Laing (1984), to understand the effects of internal Faraday rotation. Internal RM will depolarize; by the time the electric vector has rotated by one radian, the fractional polarization of the signal drops nearly to zero. In addition, internal RM causes the rotation angle χ to deviate from the usual λ^2 behavior in all geometries except the very simplest one, a resolved slab with fully uniform magnetic field direction. For $\chi \lesssim 1$, the deviations are small but measurable; for $\chi > 1$, the deviations are significant. The observed polarization angle obeys $\chi \propto \lambda^2$ very well in both sources. An RM of 100 rad/m² leads to $\chi \sim 1/3$ radian at 6 cm; one might argue that deviations of a real source from an ideal λ^2 law are small enough in this regime not to be detected. The same RM leads to $\chi \sim 3$ radian at 20 cm, which would depolarize the sources when observed at wavelength. This is not borne out by observations. Eilek *et al.* (1984) measured $\sim 20\%$ fractional polarization at 20 cm. We also have unpublished 20 cm data for 3C75 which shows similarly high polarization. Thus, it is quantitatively difficult to ascribe the RM in these two sources to internal effects.

We can also make two qualitative arguments. First, many other cluster-center radio galaxies have very high measured RM values (summarized in §4). All of these have high enough RM that the observed polarization and rotation must come from a foreground screen; internal effects as described above would depolarize the source and cause strong deviations from the λ^2 law. These clusters thus have a magnetized ICM which provides the Faraday screen. It seems simplest also to ascribe the RM in our two sources to Faraday effects from the magnetized ICM. Second, one can compare the de-rotated magnetic field vectors, in Figures 3 and 4, with the RM images, Figures 5 and 6. There is little relation in either

source between the field direction, and the RM values. If the RM were internal, we would expect the geometry of the RM image to be reflected in the geometry of the projected field. This is not the case. Thus, we conclude that the intervening magnetized plasma which causes the RM is almost certainly the ICM in the two clusters.

3. Analysis: Magnetic Fields in Cluster Centers

The data tell us that a magnetic field exists in the cores of these two clusters. In this section we consider likely field models and the magnetic field strength that each requires.

3.1. Basic Tools

We first recall the basic expression for rotation measure. Let χ be the angle of the electric vector, and λ the observing wavelength. The fundamental relation is,

$$RM = \frac{d\chi}{d\lambda^2} = \frac{e^3}{2\pi m^2 c^4} \int n \mathbf{B} \cdot d\mathbf{l} \text{ rad/m}^2 \quad (1)$$

Note that we cannot measure the full vector magnetic field, \mathbf{B} . Rather, we measure the density-weighted mean of its component along the line of sight. Expressing this numerically, and assuming a constant density over length L_{RM} , we have

$$RM \simeq 810nL_{RM}\langle B_{\parallel} \rangle \text{ rad/m}^2 \quad (2)$$

if L_{RM} is the typical length scale of the magnetized plasma along the line of sight, and $\langle B_{\parallel} \rangle$ is the weighted algebraic mean of the component of \mathbf{B} , also along the line of sight. In this expression, B is in μG , n in cm^{-3} and L in kpc. The importance of this line-of-sight averaging is that, given a density and a scale length, we are measuring only a lower limit to the magnetic field. The field is likely to have components perpendicular to the line of sight (which increases B by $\sqrt{3}$, on average, from $\langle B_{\parallel} \rangle$). In addition, any sign reversals along the line of sight also lead to a true B_{\parallel} which is larger than $\langle B_{\parallel} \rangle$.

Knowledge of the gas density is needed to interpret the RM data. X-ray data reveal the distribution of thermal gas in the cluster. Some clusters have strong X-ray peaks, in which the high gas density makes cooling important; we call these cooling cores (CC's). Other clusters have flatter central X-ray profiles, in which cooling is not important; we call these non-cooling clusters (NC's). Both cooling and non-cooling clusters show a gaseous core, of roughly constant density, and an extensive outer region of declining gas density. The two types of clusters differ only in the size and central density of the core. Eilek &

Markovic (2001) find that hydrostatic gas in a Navarro, Frenk & White (1997) potential describes the X-ray surface brightness well in both types of clusters. They give a Hubble-type approximation for the gas density,

$$n_g(r) \simeq \frac{n_o}{(1 + r/a)^x} \quad (3)$$

where the exponent $x \simeq 2.0$ for CC's and $x \simeq 2.7$ for NC's. Fits to the X-ray data show that the core radii are much smaller for CC's than for NC's: $a \sim 100$ kpc for CC's, while $a \sim 600$ kpc for NC's. The radius of the “gas core”, defined as the region within which the gas density $\gtrsim 0.2n_o$, is ~ 90 kpc for CC's, and ~ 400 kpc for NC's.

3.2. Possible Extent of the Magnetic Field

What is the spatial extent of the magnetic field which causes the RM? There are three possibilities. (1) The field may originate in the radio source itself, and be mixed with the ambient gas in a “skin” of the radio source. (2) The field may be a cluster-wide field, and the radio source simply provides a backlight to illuminate it. (3) The field may originate in a cluster-wide field, but be enhanced in the center either by a cooling-driven inflow, or by interactions of the radio source with the ambient medium. We discuss each in turn. We base our discussion on A400 and A2634, and on the full set of well-imaged cluster-center sources (reviewed in §4, below).

3.2.1. Fields in a skin of the radio source

Shortly after the first detections of high RM, Bicknell *et al.* (1990) argued that it is solely due to the radio galaxy. They proposed that surface turbulence from a Kelvin-Helmholtz instability allows diffusion of particles and fields from the low-density, radio-loud plasma into the denser ICM. The RM comes from this mixing layer. This model does not require that the cluster plasma contain any magnetic field. Other authors (Taylor & Perley 1993, Ge & Owen 1993) argued against this idea. They argued that this picture is quantitatively unlikely. The high RM in smaller sources requires either a mixing layer which is thick compared to the size of the source (unlikely on physical grounds), or a strong magnetic field in a thin mixing layer (which would be overpressured and short-lived). Taylor & Perley also point out that the RM in Hyd A is strong along the jet as well as lobes (unlikely in an instability-driven model). We also find the mixing-layer model unlikely. The RM distribution in the two sources presented in this paper seems to be influenced more by the elongation axis of the X-ray luminous gas

than the direction of the tails. This is apparent by comparing Figures 1 and 5, or 2 and 6. This suggests to us a cluster origin.

We also note geometrical arguments against the thin-skin model. (1) More cluster-center sources show asymmetric RM patterns than symmetric ones: the RM distribution and magnitude are quite different in the two lobes. As one might expect fluid instabilities to develop symmetrically in a symmetric radio source, this argues against a mixing-layer origin. (2) One might expect edge effects from this mixing layer: the RM image should be limb-brightened, or perhaps limb-darkened. We find no sign of limb effects in the RM maps of A400, A2634, or any of the other cluster-center sources. (3) There are strong suggestions of low surface brightness haloes around some Type I tails, as in Figure 2. In addition, the inner radio lobes of M87, another high-RM central source, sit in a much larger extended halo (Owen, Eilek & Kassim 2000). For such sources, the interface between the radio plasma and the ICM is not well-defined, thus shear-driven instabilities may not develop.

3.2.2. *Magnetic fields throughout the cluster*

An alternative picture is that all clusters contain magnetized plasma. Conditions derived for cluster cores (such as the order scale and fractional energy density of the field) should then be typical of the entire ICM in the cluster.

If a cluster-wide magnetic field exists, it may well have a uniform strength within the gas core, but it is very likely that the field strength falls off on larger scales. For instance, if plasma dynamics keep the pressure ratio $\beta = p_B/p_g$ constant throughout the cluster, we would have $B \propto (nT)^{1/2}$. It follows that the RM of cluster-center sources will be dominated by conditions in the gas core; outer regions of the cluster will contribute little.

We know of nothing in the data which rules this out. We will show below that the pressure ratio is typically $\beta \sim O(.1) - O(1)$ in the magnetized filaments which contribute to the observed RM. This seems inconsistent with both radio halo and statistical RM studies, which suggest μG fields, and $\beta \ll 1$ on cluster-wide scales. However, both these observations are also consistent with higher large-scale B and β values, if the high-field regions do not fully fill the ICM.

3.2.3. *Cluster-wide fields amplified by cluster-center effects*

There is a third possibility. It may be that the entire cluster plasma is magnetized, but at a lower level, so that $\beta \ll 1$. This weak, cluster-wide field could be enhanced to $\beta \sim 1$

levels in the region of the central radio source. There are two ways in which this might happen.

One way to amplify the ambient field is compression in a cooling-driven inflow. Nine of the 12 high-RM central sources sit in the centers of strong cooling cores. If the short central cooling time in these cores does lead to an inflow or collapse of gas toward the center, any flux-frozen cluster field will be amplified by the density increase (*e.g.*, Soker & Sarazin 1990, or Garasi 2001). The ambient field can also be amplified by the interaction of the central radio galaxy with the local ICM. We expect a central radio source to deposit a significant amount of energy into the local ICM. This will drive turbulence which can act as a local dynamo, amplifying the cluster-wide field to higher levels.

We know of nothing in the data which rules out this picture. It is in reasonable agreement with the radio halo and statistical RM data. Thus, we conclude that we cannot discriminate between a strong, cluster-wide field, or an enhanced cluster-center field, as the origin for the observed central Faraday rotation.

3.3. Possible Magnetic Field Geometry

The ICM magnetic field is unlikely to be uniform and unidirectional throughout the cluster. Some authors propose large-scale order; others propose small-scale randomness.

We are aware of two models which predict large-scale order in the ICM field. Soker & Sarazin (1990) proposed that a radial cooling flow would stretch out initially random, turbulent fields into approximately radial “field loops”. This structure would give a characteristic RM signature: cells of alternating RM sign (assuming the cells are resolved, so that beam depolarization is not an issue), with amplitude decreasing with projected distance away from core (as the radial field rotates away from the line of sight). We do not see evidence of this in our data. Eilek (1991) noted that a turbulent dynamo with strong helicity could maintain a field with large-scale order. The simplest solution for clusters is probably an axisymmetric field in spherical geometry. Such a field can be described as sets of toroidal flux tubes. The RM signature would be a few large-scale patches of ordered RM, both positive and negative. This is consistent with, but not required by, our data.

Alternatively, an ICM field supported by turbulence may have a disordered structure. An older approach to turbulent fields assumes many space-filling ‘cells’ (*e.g.*, Burn 1966). Such a field would result in a RM image which also appears random, with alternating “cells” of positive and negative RM. This picture does not seem consistent with our images. In addition, newer work on turbulent magnetic fields suggests a different picture. Numerical

simulations reveal that MHD turbulence is often characterized by intermittency in the magnetic field. That is, elongated, high-field flux ropes are separated by low-field regions. This geometry was discussed analytically by Ruzmaikin, Sokoloff & Shukurov (1989), and has also been seen in two- and three-dimensional MHD simulations (*e.g.*, Menguzzi, Frisch & Pouquet 1981; Biskamp 1993, §7.7; Kinney, McWilliams & Tajima 1996; Miller *et al.* 1996). The plasma density inside these flux ropes may be lower than that in the surroundings, to maintain a pressure balance. The observational signature of an intermittent field would be high-RM patches, possibly separated by lower-RM regions.

Looking to the data, we note that all of the sources show evidence of ordered RM patches, which may or may not alternate in sign, on scales $\sim 1 - 10$ kpc. This seems consistent with the intermittent field picture. In addition the larger sources (A400 and A2634, also Hyd A, Taylor & Perley 1993) show evidence of larger-scale structure: the apparent relation of the RM in A400 and A2634 to the 100-kpc scale structure of the X-ray gas core, and the side-to-side asymmetry, on a 50-kpc scale, of Hyd A. The data thus suggest a larger order scale may exist which is not sampled by the smaller sources.

To analyze our data, we therefore choose a model in which high-field flux ropes are surrounded by a lower-field background plasma. We do not have a good model for the larger order scale, but it is not critical for our analysis here. Our images of A400 and A2634 show patches with scales ~ 10 kpc, which we identify as the transverse size of the flux ropes. We note that such a geometry can have a large (area) covering factor while having a small (volume) filling factor. To show this, let the filaments have radius r and length L , and immerse N filaments in a region of radius R (the gas core). The covering factor is the ratio of projected filament area to total projected area: $cf \simeq NrL/R^2$. The fractional volume occupied by the filaments is the filling factor, $ff \simeq Nr^2L/R^3$. The lack of low-RM holes in the images requires that $cf \gtrsim 1$; this is consistent with $ff \lesssim 1$ when $r < R$.

4. Results: Magnetic Field in Cluster Cores

In this section, we first analyze the field in our two clusters. We then put our results in the context of all nearby cluster-center sources which have been studied in RM.

4.1. The Magnetic Field in A2634 and A400

We refer to Table 1 to estimate the characteristic density and temperature in the inner $\lesssim 100$ kpc of each cluster. For Abell 400, we take $n \simeq 0.0021 \text{ cm}^{-3}$, and $T \simeq 1.5 \text{ keV}$; for

Abell 2634 we take $n \simeq 0.0016 \text{ cm}^{-3}$, and $T \simeq 1.5 \text{ keV}$. Referring to figures 7 and 8, we take 50 rad/m^2 as a typical RM for A400, and 65 rad/m^2 as typical for A2634.

4.1.1. The Typical Magnetic Field

We explore three simple pictures: a thin skin on the radio source, a single magnetic feature somewhere in the region of the source, and a fully magnetized cluster core. For each picture, we use equation (2) to derive $\langle B_{\parallel} \rangle$, using the typical X-ray gas densities given above. We estimate the magnetic pressure as $p_B \simeq 3\langle B_{\parallel} \rangle^2/8\pi$, and compare it to the gas pressure, $p_g = nk_B T$. Our results for each model are summarized in Table 2.

We start by testing the model in which the RM arises from a skin of the radio source, in which magnetic field from the source has mixed with ambient ICM. We take the skin thickness to be 10% of a typical radius of the radio tail, and we estimate the latter very simply from the inspection of the radio images. For 3C75 we take $L_{RM} \sim 1.2 \text{ kpc}$, and for 3C465 we take $L_{RM} \sim 0.7 \text{ kpc}$. From the results in Table 2, we see that this picture requires quite high fields, of order tens of μG . Such strong fields would be at a much higher pressure than the ambient gas, indicating that such a shell is unlikely to be long-lived.

It seems more likely that the magnetic field is associated with the X-ray loud gas in the cluster core. In this case, we assume magnetic field is intermittent, with filament radius equal to the projected scale on which the RM is ordered. We thus take $L_{RM} \sim 10 \text{ kpc}$ for A400, and $L_{RM} \sim 20 \text{ kpc}$ for A2634. We cannot predict the filling factor for the magnetic features. We therefore use the two extremes of a single filament along the line of sight, and a fully filled core. A single filament requires a field $\sim 2 - 3 \mu\text{G}$ in each case, and predicts a magnetic pressure which is interestingly close ($\sim 60\%$) to the thermal pressure in each case. The other extreme assumes a filled core. Comparing the gas core radii (300 kpc for A400, 400 kpc for A2634) to the filament diameters, and assuming the interfilament distance is a few times the filament diameter, we estimate typically $O(10)$ filaments would lie along the line of sight through each core. The most probable observed RM will be the RM of a typical magnetic feature, increased by the square root of the number of such features superimposed along the line of sight. In this case, the magnetic field is reduced by a factor of $\sqrt{10}$, and the pressure ratio by a factor of 10, compared to the single-filament case. This limit reduces the magnetic pressure to a few percent of the thermal pressure. Both limits are shown in Table 2.

4.1.2. Extrema and Gradients in the RM

We used the arguments above to estimate “typical” RM values and magnetic field strength. Two further points are worth noting.

First, the RM is not uniform in either object; local, high-RM patches can be found (Figures 9 and 10). These patches are not generally associated with any significant feature in the radio-loud plasma. These patches have larger RM, and smaller size, than is typical of the rest of each source. To analyze this, we assume these patches are unique features projected on the source, with line-of-sight scale equal to transverse scale. We take $L_{RM} \sim 10$ asec ~ 4.4 kpc for A400 and $L_{RM} \sim 7$ asec ~ 4.1 kpc for A2634. This gives the final numbers in Table 2; we see that high fields are required here. Unless these extrema have an unusual geometry (with line of sight depth greater than their transverse scale) we find that they must be strongly overpressured regions. It follows either that they are magnetically self-confined, or that they are short-lived compared to the age of the radio galaxy.

Second, the mean magnitude of the RM does not decay with radius as rapidly as the density of the X-ray gas. We can see this by comparing Figures 7 and 8 to Table 1. For A400, the RM stays at a constant magnitude, while the density drops by a factor of ~ 4 over the inner 100 kpc, and the projected column density drops by a factor ~ 2 over the same range. For A2634, the RM drops by a factor $\lesssim 3$ in the inner 100 kpc, while the density drops by ~ 8 and the column density by a factor ~ 5 . Thus, in each cluster the value of $\langle B_{\parallel} \rangle L$ must increase, by a factor of a few, over the inner ~ 100 kpc.

4.2. Comparison to Other Cluster-Center Sources

We thus conclude that magnetic fields play a significant role in the cores of A400 and A2634. Most imaging of cluster-center RM up to now has addressed smaller linear sizes and strong cooling cores. Comparing our two clusters to the full set studied so far shows that significant magnetic fields are common in cluster cores, whether or not cooling is important. To demonstrate this, we have combined our data with all published RM images of nearby cluster center sources. This gives us a set of 12 nearby clusters (we exclude high-redshift objects due to poorer knowledge of the gas distribution). Our compilation is similar to that of Taylor *et al.* (1999), but we consider only cluster-center sources, and carry out a different analysis.

4.2.1. Magnetic Field Analysis

Given the variety of resolution of the RM images and, especially, of the X-ray images of the sources, we have only attempted a “low resolution” treatment. We repeat the analysis of §4.1.1, using X-ray data to estimate the gas density and temperature which are “typical” of the volume close to the radio source. We assume that one filament, with transverse scale $\sim L_{RM}$, lies along the line of sight. The smaller cores typical of these clusters make it unlikely that more than a few such flux ropes lie along the line of sight. We put our detailed assumptions, and specifics for each cluster, in the Appendix. In Table 3 we list for each source: the linear size of the radio source over which RM has been measured, D ; the strength of the cooling core, estimated by \dot{M} , the mass inflow rate in a traditional cooling-flow analysis; the typical RM value; the scale length over which the RM is ordered; the typical density and temperature for the X-ray gas; our results for $\langle B_{\parallel} \rangle$; and our derived ratio of magnetic pressure to gas pressure.

Table 3 shows that there is a clear trend for the magnetic field to be significant in these clusters. All but three of the sources have $p_B/p_g \gtrsim 0.1$, which we consider a reasonable threshold for the magnetic field to have some importance in the gas dynamics. Three of the sources even have $p_B \geq p_g$. Thus, we conclude the magnetic field is generally important in these cluster cores, and that $p_B/p_g \sim O(0.1) - O(1)$ is a “typical” value of the pressure ratio in the high-field filaments.

Table 3 also shows that the magnetic field correlates with the gas density in the core. This is a stronger result than a correlation of the RM with the density. The correlation of B with density shows that the magnetic field is closely connected to the dynamics of the ICM. We return to this below, when we consider how the field is maintained.

4.2.2. Caveats

It is worth pointing out the uncertainties in our “low resolution” estimates of the cluster-center magnetic fields.

First, the X-ray deprojections contain uncertainties. The deprojected densities should be fairly robust, on and above the beam size. X-ray emissivities are not very sensitive to temperature, for gas above $\sim 10^7$ K, and the clusters in question do not deviate significantly from approximate sphericity. On scales less than the beam size, where we had to estimate the density enhancement around a small radio source and ignore central asymmetries, our numbers are of course less reliable. In addition, the local temperature is uncertain. This is true because because older published work only gives a mean temperature for the cluster,

and because cooler gas in the cluster core can be hidden in the final X-ray image. Thus, the central temperature, and thus gas pressure, may be significantly less than our estimates here. This would increase the plasma $\beta = p_B/p_g$.

Second, we assumed the simplest geometries in deriving magnetic field values. We assumed a unity covering factor for magnetic features. This can lead to an overestimate of the field strength. In addition, we assumed the X-ray gas is well mixed in the high-field filaments. This may not be the case, as magnetized filaments may expel plasma in order to stay in pressure balance with their surroundings. This effect will give larger field values than we have estimated. Finally, we have used a “typical” RM value for each source; this ignores the smaller, high-RM patches which exist in several of the sources. As with A400 and A2634, high-field patches may also exist in these clusters.

5. What Maintains the Magnetic Field?

We have shown that strong magnetic fields, $\beta \lesssim 1$, are common in the centers of rich clusters. These fields require a driver. The small order scale, $\lambda_t \sim 10$ kpc, means that reconnection will dissipate the field on a time $\tau_A \sim 10\lambda_t/v_A$, if $v_A = B/(4\pi\rho)^{1/2}$ is the Alfvén speed (*cf.* Parker, 1973, or Garasi, 2001). $\tau_A \sim 100$ Myr for typical cluster conditions. Thus, magnetic driving is needed; turbulence in the ICM is the most likely mechanism. We also note the correlation of the magnetic field and gas density (in Table 3) strongly suggests a dynamical connection between the field and the thermal plasma. We need to understand what drives the turbulence.

5.1. Turbulent support of magnetic fields

We summarize the important parameters which allow quantitative estimates of turbulent driving. Let v_t be the characteristic turbulent velocity, and λ_t be the characteristic scale, probably the scale on which the turbulence is driven. $E_t \simeq \rho v_t^2 V$ is the turbulent energy in volume V . Let P_t be the driving power for that volume. Viscous effects will dissipate the turbulence on a time $\tau_t \sim \text{few} \times \lambda_t/v_t$. For times $t < \tau_t$, the turbulent energy $E_t \sim \int P_t dt \sim P_t t$; for times $t > \tau_t$, the system reaches a balance at $E_t \sim P_t \tau_t$. For transonic turbulence, on small scales (say, $\lambda_t \sim 10$ kpc), the decay time $\tau_t \sim 50 - 100$ Myr; thus small-scale turbulence must be continually replenished. Alternatively, if $\lambda_t \sim \text{Mpc}$, as in merger driving (*e.g.*, Norman & Bryan 1999, or Roettiger *et al.* 1997) we would not expect energy balance to be established.

If the turbulent fluid is a magnetized plasma, the mean magnetic field will be amplified to approximate dynamic balance,

$$B^2 \lesssim 4\pi\rho v_t^2 \quad (4)$$

This process needs only a very small seed field. Early-epoch galaxy activity is a possible source for seed fields (*e.g.*, Kronberg *et al.* 1999, Völk & Atoyan 1999), as is wind ejection from normal galaxies at the present epoch. Note that the high fields we find in cluster cores, with $B^2 \sim 8\pi p_g$, require that the turbulence be transonic. Simulations (De Young 1980, 1992) show that the rate at which dynamo amplification happens depends on the nature of the turbulence. The helicity of the turbulence is critical here. (Helicity is defined as $\mathbf{v} \cdot \nabla \times \mathbf{v}$; a tornado, with flow along its rotation axis, is a dramatic example of helical flow). Simulations show that simple, isotropic (non-helical) turbulence takes many characteristic times (30 - 100) to establish this balance. Strongly helical turbulence is faster, establishing dynamical balance in $\sim \tau_t$. The spatial structure of the field also depends on the structure of the turbulence. Isotropic, non-helical turbulence amplifies the magnetic field on scales no larger than the driving scale. Such turbulence is probably intermittent, containing thin, high-field flux ropes. Helical turbulence leads to strong fields which are ordered on scales $\gtrsim \lambda_t$ (although it can take much longer than τ_t for significant power to cascade to these long scales). We cannot easily predict the amount of helicity in cluster turbulence, although we expect some due to galaxy rotation and to angular momentum associated with the cluster formation process.

5.2. Maintaining a cluster-wide field

5.2.1. Galaxy Driving

The motions of galaxies through the ICM will heat the ICM, and will drive turbulence in the ICM at some level. That turbulence will support amplify an initial seed field to approximate equipartition levels, as in (4). As this must be occurring in all clusters, it provides the minimum turbulent and field levels to be expected. These levels turn out to be very weak.

We estimate the energetics as follows. Say that N_g bright galaxies (close to L_*) occupy a cluster core. They transfer energy to the ICM over their gravitational radius, $r_g \sim 5$ kpc (for $M_g \sim 10^{12} M_\odot$, and $v_g \sim 10^3$ km/s). The rate of energy transferred to the ICM will be $\rho v_g^3 \pi r_g^2$, times some efficiency ϵ . If we assume energy equipartition, $M_g v_g^2 \simeq \text{constant}$, we find a driving power that is a strong function of galaxy mass: $P(M_g) \simeq \pi \epsilon \rho G^2 M_g^2 / v_g$.

We can include a distribution of galaxy masses. We take $N(M_g) \propto M_g^{-5/4}$, $M_g < M_*$,

if $M_* \sim 10^{12} M_\odot$ is the cutoff mass. The total number of galaxies is $N_g = \int N(M_g) dM_g$. Energy equipartition gives $v_g(M_g) \sim \sigma(M_*/M_g)^{1/2}$, where σ is the cluster velocity dispersion. The net driving power is then

$$P_g = \int_0^{M_*} N(M_g) P(M_g) dM_g \simeq \frac{\pi}{9} \epsilon N_g \frac{\rho}{\sigma} G^2 M_*^2 \quad (5)$$

We estimate the steady-state turbulence level by balancing this driving against dissipation:

$$P_g \simeq P_t \simeq \frac{\rho v_t^3}{\lambda_t} \quad (6)$$

This relation gives us an estimate of the turbulent energy density, ρv_t^2 . From this, using (4), we find the mean magnetic field that can be maintained by galaxy driving:

$$B \simeq 0.26 n_e^{1/2} (\epsilon N_g)^{1/3} \left(\frac{M_{12} \lambda_{10}}{\sigma_e} \right)^{1/3} \mu\text{G} \quad (7)$$

To put in numbers, we consider a very rich cluster, to make the best case for galaxy driving. We pick $n_3 = M_{12} = \lambda_{10} = \sigma_e = 1$, and $\epsilon N_g = 10$. This last is meant to describe a rich cluster with moderate efficiency. Under these conditions, we estimate that galaxy driving will maintain turbulent velocities $v_t \sim 40 \text{ km/s}$, and $B \sim 0.5 \mu\text{G}$. This result shows (in agreement with some previous authors: Goldman & Raphaleli 1991, De Young 1992), that only a very small mean field can be maintained by galaxy-driven turbulence.

5.2.2. Driving by cluster relaxation and mergers

An alternative to galaxy driving is that the magnetic field is maintained by turbulence driven by ongoing mergers. There is substantial evidence that not all clusters are quiescent and dynamically relaxed. Many are still evolving dynamically, and some are undergoing dramatic major mergers at the present epoch. In addition, simulations suggest that minor mergers are common, with infalling matter still accumulating into the potential wells of large clusters.

This can be a much stronger driver than the motion of individual galaxies. Norman & Bryan (1999) suggest 10^{62} erg for the kinetic energy of infalling subclusters in their “minor merger” simulations. This value is comparable to the internal energy of a rich cluster, and much greater than the energy supplied by galaxy driving (equation 5) over the life of the cluster. A cluster with a recent merger may still contain several high-velocity clumps. Each such clump will energize the ICM in the same way as a large galaxy will, but at higher levels.

Mergers have also been suggested as the answer to a problem posed by Eilek *et al.* (1984), and Owen *et al.* (1985). These papers showed that the the radio sources in A2634 and A400 cannot be bent by the motion of their parent galaxies relative to a static ICM in a static cluster potential. The situation could be resolved if the ICM exhibits large-scale transonic flows, such as can be attained in a favorable merger event (Roettiger *et al.* 1997). It may be that these clusters have undergone merger events fairly recently, and that turbulence driven by the merger is responsible for the magnetic fields therein.

Thus, it is plausible that ongoing mergers drive cluster-wide turbulence strongly enough to maintain transonic turbulence, and dynamically significant magnetic fields, throughout the cluster. We caution, however, that this hypothesis has not yet been established quantitatively. Mergers occur on large scales (\sim Mpc). We would expect the characteristic size of merger-driven turbulence to be large as well. This seems to conflict with the data which show ~ 10 kpc order scales in the RM, suggesting significant turbulent power on these scales. It has not yet been established whether or not merger-driven turbulence can cascade effectively to these scales. (Numerical simulations are not yet able to evaluate turbulent and magnetic field levels on scales small compared to the cluster or merger; they are limited both by finite resolution and by the difficulty of including dissipative and resistive effects). Another concern is that many of the clusters with high RM values and high B fields, also contain strong cooling cores. There are problems with the suggestion that these clusters have recently undergone significant mergers. A strong merger will heat the central ICM (as in Roettiger *et al.* 1997, or Schindler & Prieto 1996), and disturb the underlying gravitational potential. It is not obvious that the relaxed profiles and lower central temperatures characteristic of cooling cores are compatible with recent mergers in these clusters.

5.3. Cluster Core Amplification

5.3.1. Cooling Flows as a Driver

Another possibility is suggested by the fact that most of the sources in Table 3 sit in the center of strong cooling cores. It may be that the high magnetic fields in these clusters are local to the cluster core, and are due to a cooling flow. If such flows exist, they will enhance an initially weak magnetic field by simple compression. Soker & Sarazin (1990) found that an initial field at the μ G level would reach dynamic balance within the inner ~ 10 kpc of a standard cooling-flow model. Recent numerical simulations, such as the one-dimensional, tangled-field models of Garasi (2001), find that fields on the order of tens of μ G are very possible in strong cooling cores.

Field enhancement by a cooling-driven inflow may indeed be important in some of the high-RM clusters. However, we do not believe that current models of quasi-spherical cooling flows can explain all the data. Three of the sources in Tables 3 and 4, including the two new new sources in this paper, are not in strong cooling cores. There may be a small X-ray excess in the very inner region of both A400 and A2634; but there is no evidence for a cooling inflow on the ~ 100 kpc scale where RM is observed, and significant fields are inferred, in these two clusters.

Furthermore, it is becoming less clear that simple, slow inflows described in current models really characterize clusters with cooling cores. As we describe in the next section, evidence is accumulating that active central galaxies deposit a significant amount of energy into the cluster core. Such energy input will heat and disturb the gas, providing both kinematic and magnetic pressure support, and possibly leading to a cycle of infall and outflow (regulated by the lifetime of the radio source), on times short compared to the life of the cluster (*e.g.*, Binney 1999). Thus, a cooling-driven collapse may contribute to the magnetic fields seen in many of the clusters studied do far, but we do not think it is the full solution.

5.3.2. *The radio source as a driver*

High magnetic fields can also be local to the cluster core is if they are maintained by the radio galaxies themselves. Recent X-ray work provides clear evidence of such interaactions. Examples are 3C388 in A2199 (Owen & Eilek 1998), M87 (Owen *et al.* 2000; Harris *et al.* 2000), or Hydra A (McNamara *et al.*, 2000). Energy arguments, presented below, show the radio source can have significant impact on the local ICM. The connection will be hydrodynamic: the radio-jet plasma will deposit energy into the local ICM, both as heat and as bulk kinetic energy (“turbulence”). Such radio-source-driven turbulence can act as a local dynamo, amplifying the cluster-wide field to larger levels. This may be the origin of the $\beta \sim 1$ fields found near cluster-center sources.

In order to test this idea, we carried out simple sums for the set of ten sources in Table 3. We compiled radio data from the literature: the largest size, D , over which RM has been measured; the bolometric radio power P_{rad} (assuming a 10 MHz - 10 GHz band); and the minimum pressure internal magnetic field, B_{mp} (although the diversity of observations and resolution makes this quantity only a very approximate measure of the internal energy density of the sources). These quantities are listed in Table 4; details and references are in the Appendix). Table 4 shows that B_{mp} and $\langle B_{\parallel} \rangle$ are somewhat correlated. This suggests an approximate dynamic balance between the pressures inside the radio source and in the local ICM.

One could also explore this picture by considering timescales. Let the radio beam carry power P_b , and assume most of this is deposited in the local ICM. It is simple to determine how long it takes for the beam to deposit an amount of energy equal to the total thermal energy in the central volume *for which the RM has been measured* (this last is a minimum energy requirement). This is,

$$\tau_E = (8\pi/3)nk_BTD^3/P_b \quad (8)$$

We assume the radio jet carries total beam power $P_b = 100P_{rad}$. The final column of Table 4 shows that this times can be short. The smaller sources, with their smaller associated volumes, have $\tau_E \sim$ few Myr. This is quite a short time; one would clearly expect these sources to affect their immediate surroundings. The two largest ones have $\tau_E \sim 200 - 300$ Myr. This is a longer time, but not significantly longer than the ages estimated for large, tailed radio galaxies. Thus, it may be that the high magnetic fields we observe are only local to the cluster core, and are maintained by turbulence which is driven by the radio galaxy itself.

6. Summary and Conclusions

In this paper we have combined new and existing Faraday rotation data to study the magnetic field in the cores of clusters of galaxies.

We presented new observations of two large, tailed radio galaxies at the center of non-cooling clusters. We used these data together with X-ray data to estimate the field strength, and found dynamically interesting fields exist in the inner ~ 100 kpc of A400 and A2634. We also used data from the literature to carry out a simple RM analysis for the 12 clusters with RM data for cluster-center sources. We found that significant magnetic fields (with $\beta \sim 0.1 - 1$) are common in cluster cores. In our analysis we assumed the magnetic field has a filamentary structure, and that the RM is dominated by the high-density (and probable high-field) gas core of the cluster.

We then considered possible origins and drivers for the field. Galaxy motion is only a weak driver. The turbulence that galaxies create in the ICM may maintain fields at a sub-microgauss level, but cannot account for the stronger fields detected in rotation measure. We do find three possible mechanisms to support the larger fields.

1. Ongoing mergers, at least minor ones, are likely in many clusters. Such mergers should be able to drive strong turbulence in the ICM, and thus maintain interesting levels of magnetic field. The asymmetric inner gas distribution in A400 and A2634 may be due to recent merger activity in these two clusters. We caution, however, that this model cannot

easily be quantified to predict specific field levels; and note that it may not explain the fields found in strong cooling cores.

2. Cooling-driven collapse of the ICM can amplify a weaker cluster-wide field in the central cooling core. As previous authors have noted, this may account for the high fields found in the cooling cores previously studied. It clearly is not relevant, however, to the two clusters presented in this paper, which do not sit in cooling cores.

3. The central radio galaxy may also play a role in maintaining a strong local field. Some part of the jet power will be deposited in the nearby ICM, driving turbulence as well as heating that ICM. Simple energetic considerations show that strong turbulence, and field, levels are possible local to the radio source.

We cannot discriminate between these three models. We suspect that all are operating at some level, in at least some clusters. What we can conclude is that the intracluster plasma is not as simple as many of us once thought.

We are pleased to acknowledge stimulating conversations with Tracy Clarke, Dave De Young, Chris Garasi, Tomislav Markovic, and Mark Walker, over the course of this work. Comments from an anonymous referee improved the structure and organization of the paper. We are also grateful to Paddy Leady for the initial stimulus to carry out the observations, and to Qiang Wang for help with the X-ray data. This work was partially supported by NSF grant AST-9720263.

A. X-ray Analysis and Individual Clusters

We have detailed X-ray deprojections for the two sources in this paper, for A2199 from Owen & Eilek (1998), and for M87 (Owen, Eilek & Kassim 2000). The extent of the radio sources sampled by Faraday rotation in A400, A2199 and A2634 is larger than the X-ray beam. For these sources we used the deprojections to estimate “typical” densities across the RM region. The extent sampled in RM in M87 and in the 3C129 cluster are comparable to the X-ray beam, so we used the central density from deprojections in the literature. For the other 7 sources, we have only published X-ray analyses. These give X-ray temperature, and also either the gas density in the central X-ray bin, or the cooling time in that bin (which, with an assumed temperature, can be converted to number density; we use the analytic cooling curve of Westbury & Henriksen 1992 to do this). All of these sources are smaller than the X-ray resolution element, and all are in strong cooling cores. The local gas density at the radio source will thus be larger than the mean over the X-ray beam. To estimate this

correction, we used the cooling-cluster density models of Eilek & Markovic(2001), and the estimated size scale of the X-ray gas for each particular cluster, as described in that paper. Our estimated corrections were factors from 2 to 4 in all cases. Finally we converted all estimates to our assumed $H_o = 75$ km/s-Mpc.

In the following we give relevant details for each cluster. We use the following abbreviations: KPTW, Kellerman, Pauliny-Toth & Williams (1969); ES91, Edge & Stewart (1991); ESF92, Edge, Stewart & Fabian 1992; W97, White *et al.*(1997); P98, Peres *et al.*(1998).

Abell 400 contains 3C75, a Wide-Angle Tail radio source. KPTW give fluxes and spectral indices; the source can be fitted by a single power law, $\alpha = -d \ln S_\nu / d \ln \nu \simeq 0.8$ from 10 MHz to 10 GHz. Owen *et al.* (1985) present the radio image; the Faraday data and cluster magnetic fields are discussed in the present paper. Beers *et al.* (1992) present EINSTEIN data; the ROSAT data is presented in this paper. In §4 we take the typical $T \sim 1.5$ keV. This cluster has a broad gas core, making it a non-cooling cluster, but also has a weak central X-ray excess which may be a small cooling core.

Abell 1795 contains the tailed radio source 4C46.42. van Breugel, Heckman & Miley (1984) present radio fluxes and estimate $\alpha \simeq 1.0$ over the radio range. Ge & Owen (1993) present the radio image and Faraday rotation data. We use X-ray data from P98, W97, ES91; and estimate the density close to the radio source ~ 4 times the mean density in the inner (IPC, PSPC) X-ray beam.

Abell 2052 contains the diffuse radio source 3C317. Zhou *et al.*(1993) compile fluxes, and KPTW give $\alpha \simeq 0.92$ at low frequencies; the source steepens above ~ 300 MHz. Ge & Owen (1994) present a radio image, as do Zhou *et al.*. We use X-ray deprojections from W97, P98, and estimate the density close to the radio source ~ 2.4 times the mean density in the inner (IPC, PSPC) X-ray beam.

Abell 2029 contains a tailed radio source, PKS 1508+059. Arnaud (1985), also Jones & Forman (1984) use EINSTEIN data to estimate gas densities and temperature. Recent radio data are presented by Taylor, Barton & Ge (1994), who also discuss the cluster magnetic field. This is a steep spectrum source, $\alpha \simeq 1.5$ down to 80 MHz (Taylor *et al.* 1994). We use X-ray deprojections from ES91, ESF92, and P98, and estimate the density close to the radio source ~ 2 times the mean density in the inner (IPC, PSPC) X-ray beam.

Abell 2199 contains the diffuse radio source 3C338. KPTW give fluxes; this is a steep spectrum source, $\alpha \simeq 1.09$ at low frequencies. Ge & Owen (1994) present the radio image.

Owen & Eilek (1998) present and deproject ROSAT data and use Faraday data to infer the magnetic field. We use their X-ray deprojection, and estimate $T \sim 2$ keV based on Thomas, Fabian & Nulsen (1987).

Abell 2634 contains 3C465, a Wide-Angle Tail radio source. The spectrum can be described by a single power law, $\alpha \simeq 0.8$ (KPTW). Eilek *et al.* (1984) present radio images and the EINSTEIN data; the Faraday data and ROSAT data are discussed in the present paper. In §4 we take the typical $T \sim 1.5$ keV. This cluster has a broad gas core, making it a non-cooling cluster, but also has a weak central X-ray excess which may be a small cooling core.

Abell 3526 is also called the Centaurus cluster. The small, tailed radio source 1246-410 is associated with the central galaxy. Taylor *et al.* (1999) present the radio image, which suggests that the faint radio tails extend beyond the detected limits, and also the RM. We have not found other radio data; we assume the total flux is twice that given by Taylor *et al.* and $\alpha \simeq 1.0$ between 10 MHz and 10 GHz to estimate total power. The X-ray data is from P98 and Churazov *et al.* (1999).

Abell 4059 contains a tailed radio source PKS 2354-350. Taylor *et al.* (1994) present radio data; this is a steep spectrum source, $\alpha \simeq 1.43$ down to 30 MHz. Schwarz *et al.* (1991) present EINSTEIN X-ray data. We use X-ray deprojections from ES91, ESF92, P98, and estimate the density close to the radio source to be ~ 2 times the mean density in the inner (IPC, PSPC) X-ray beam.

The 3C129 cluster contains 3C129.1, a small tailed radio source associated with the central cD galaxy, in addition to the famous tailed source 3C129. We consider the former source. Taylor *et al.* (2001) present 5 GHz radio data and RM data. We use the NVSS to estimate total flux at 1.4 GHz, assume $\alpha = 1.0$ between 10 MHz and 10 GHz to estimate total radio power. The X-ray data are from W97, Taylor *et al.*; see also Leahy & Yin (2000). This cluster has a broad gas core, making it a non-cooling cluster, but also has a weak central X-ray excess which may be a small cooling core.

Cygnus A is a classical double radio source in the center of an anonymous cluster. It can be described approximately by a power law with $\alpha \simeq 0.66$ below ~ 2 GHz, and appears to turn over around ~ 25 MHz (Parker 1968; Baars & Hartsuijker 1972). Dreher, Carilli & Perley (1987) present the Faraday rotation data, and discuss cluster magnetic fields (for radio images, *cf.* Perley, Dreher & Cowan 1984). We use X-ray deprojections from ES91,

W97, P98, and estimate the density close to the radio source to be the mean density in the inner (IPC, PSPC) X-ray beam.

Hydra A is a tailed radio source in the center of an anonymous cluster. Taylor *et al.* (1990) present the radio data; Taylor & Perley (1993) discuss the cluster magnetic fields. Fomalont (1971) gives a 1400 MHz flux. The spectrum is a steady power law, $\alpha \sim 0.9$, over the radio range (Taylor 2000, private communication). We use X-ray deprojections from ES91, ESF92, P98, and estimate the density close to the radio source to be the mean density in the inner (IPC, PSPC) X-ray beam.

Virgo A is the central radio source (M87) in the Virgo cluster. Its spectrum is a good power law, $\alpha \sim 0.8$ throughout the radio range (*e.g.*, KPTW). To be consistent with our application here, we do not include flux above 10 GHz; thus our bolometric power is smaller than that quoted by Turland (1975), who extrapolates to 10^{15} Hz. Recent radio images of the inner halo are in Hines, Owen & Eilek (1989); Owen Eilek & Keel (1990) presented the Faraday image of the inner halo and used EINSTEIN data to infer the magnetic field. Nülsen & Bohringer (1995) present and deproject ROSAT PSPC data; Owen *et al.* (2000) convert their results to $H_o = 75$ km/s-Mpc, which we use here.

REFERENCES

Arnaud, K., 1985, Ph.D thesis, Cambridge University

Baars, J. W. M. & Hartsuijker, A. P., 1972, A&A, 17, 172

Balcells, M., Morganti, R., Osterloo, T., Perez-Fournon, I. & Gonzalez-Serrano, J. I., 1995, A&A, 302, 665

Beers, T. C., Gebhardt, K., Huchra, J. P., Forman, W., Jones, C. & Bothun, G. D., 1992, ApJ, 400, 410

Bicknell, G. B., Cameron, R. A. & Gingold, R. A., 1990, ApJ, 357, 373

Binney, J., 1999, in H.-J. Röser & K. Meisenheimer, eds., *The Radio Galaxy M87*, 116

Biskamp, D., 1993, *Nonlinear Magnetohydrodynamics*, (Cambridge: Cambridge University Press).

Burn, B. J., 1966, MNRAS, 133, 67

Churazov, E., Gifanov, M., Forman, W. & Jones, C., 1999, ApJ, 520, 105

Clarke, T. E., Kronberg, P. P. & Böhringer, H., 2001, ApJ, 547, 111

De Young, D. S., 1980, ApJ, 241, 81

De Young, D. S., 1992, ApJ, 386, 464

Dreher, J. W., Carilli, C. L. & Perley, R. A., 1987, ApJ, 316, 611

Edge, A. C. & Stewart, G. C., 1991, MNRAS, 252, 414

Edge, A. C., Stewart, G. C. & Fabian, 1992, MNRAS, 258, 177

Eilek, J. A., 1991, in M. Colless, A. Babul, A. Edge, R. Johnstone, & S. Raychaudhury, eds., *Clusters and Superclusters of Galaxies: Contributed Talks and Poster Papers* (NATO Advanced Study Institute), 109

Eilek, J. A., Burns, J. O., O'Dea, C. P. & Owen, F. N., 1984, ApJ, 278, 37

Eilek, J. A. & Markovic, T., 2001, in preparation.

Fabian, A. C., Hu, E. M., Cowie, L. L. & Grindlay, J., 1981, ApJ, 248, 47

Feretti, L., 1999, in Böhringer, H., Feretti, L. & Schuecker, P., eds., *Diffuse Thermal and Relativistic Plasma in Galaxy Clusters* (MPE Report 271), 3

Feretti, L., & Giovannini, G., 1996, in IAU Symposium 175, *Extragalactic Radio Sources*, eds. R. Ekers, C. Fanti, & L Padrielli (Kluwer), 333

Fomalont, E. B., 1971, AJ, 76, 513

Fusco-Femiano, R., Dal Fiume, D., Feretti, L., Giovannini, G., Grandi, P., Matt, G., Molendi, S., & Santangelko, A., 1999, *ApJLett*, 513, L21

Fukazawa, Y., Makishima, K., Tamura, T., Ezawa, H., Xu, H., Ikebe, Y., Kikuchi, K. & Ohashi, T., 1998, *PASJ*, 50, 187

Garasi, C., 2001, PhD thesis, New Mexico State University

Ge, J. P. & Owen, F. N., 1993, *AJ*, 105, 778

Ge, J. P. & Owen, F. N., 1994, *AJ*, 108, 1523

Goldman, I. & Rephaeli, Y., 1991, *ApJ*, 380, 344

Harris, D. E., Owen, F., Biretta, J. A. & Junor, W., 1999, in Böhringer, H., Feretti, L. & Schuecker, P., eds., *Diffuse Thermal and Relativistic Plasma in Galaxy Clusters* (MPE Report 271), 111

Hennessy, G., Owen, F. N. & Eilek, J. A., 1989, *ApJ*, 347, 144

Henriksen, M., 1998, *PASJ*, 50, 389

Hines, D. C., Owen, F. N. & Eilek, J. A., 1989, *ApJ*, 347, 713

Jones, C. & Forman, W. 1984, *ApJ*, 276, 38

Kellerman, K., Pauliny-Toth, I. I. K. & Williams, P. J. S., 1969, *ApJ*, 157, 1 (KPTW)

Kim, K.-T., Tribble, P. C., & Kronberg, P. P., 1991, *ApJ*, 379, 80

Kinney, R., McWilliams, J. C., & Tajima, T., 1995, *Phys. Plasmas*, 2, 3623

Kronberg, P. P., Lesch, H. & Hopp, U., 1999, *ApJ*, 511, 56

Laing, R., 1984, in A. H. Bridle & J. A. Eilek, eds., *Physics of Energy Transport in Extragalactic Radio Sources* (NRAO: Green Bank), 90

Lauer, T., 1988, *ApJ*, 325, 49

Leahy, D. A. & Yin, D., 2000, *MNRAS*, 313, 617

McNamara, B. R., Wise, M., Nulsen, P. E. J., David, L. P., Sarazin, C. L., Bautz, M., Markevitch, M., Vikhlinin, A., Forman, W. R., Jones, C. & Harris, D. E., 2000, *ApJLett*, 543, L135

Menguzzi, M., Frisch, U. & Pouquet, A., 1981, *Phys Rev Lett.*, 47, 1060

Miller, R. S., Mashayek, F., Adumitroale, V. & Givi, P., 1996, *Phys. Plasmas*, 3, 3304

Navarro, J. F., Frenk, C. S. & White, S. D. M., 1997, *ApJ*, 490, 493

Norman, M. & Bryan, G., 1999, in H.-J. Röser & K. Meisenheimer, eds., *The Radio Galaxy M87*, 106

Nulsen, P. E. J. & Böhringer, H., 1995, MNRAS, 274, 1093

Owen, F. N., Morrison, G. & Voges, W., 1999, in Böhringer, H., Feretti, L. & Schuecker, P., eds., *Diffuse Thermal and Relativistic Plasma in Galaxy Clusters* (MPE Report 271), 9

Owen, F. N. & Eilek, J. A., 1998, ApJ, 493, 73

Owen, F. N., Eilek, J. A. & Kassim, N., 2000, ApJ, 543, 611

Owen, F. N., Eilek, J. A. & Keel, W. C., 1990, ApJ, 362, 449

Owen, F. N., O'Dea, C. P., Inoue, M. & Eilek, J. A., 1985, ApJ, 294, L85

Parker, E. A., 1968, MNRAS, 138, 407

Parker, E. N., 1973, ApJ, 180, 247

Peres, C. B., Fabian, A. C., Edge, A. C., Allen, S. W., Johnstone, R. M., & White, D. A., 1998, MNRAS, 298, 416

Perley, R. A., Dreher, J. W. & Cowan, J. J., 1984, ApJ, 285, L35

Pinkney, J., Rhee, G., Burns, J. O., Hill, J. M., Oegerle, W., Batuski, D. & Hintzen, P., 1993, ApJ, 416, 36

Roettiger, K., Loken, C. & Burns, J. O., ApJS, 109, 307

Ruzmaikin, A., Sokoloff, D. & Shukurov, A., 1989, MNRAS, 241, 1.

Schwartz, D. A., Bradt, H. V., Remillard, R. A. & Tuohy, I. R., 1991, ApJ, 276, 424

Schindler, S. & Prieto, M. A., 1996, A&A, 327, 37

Scudeglio, M., Solanes, J. M., Giovanelli, R. & Hanyes, M. P., 1995, ApJ, 444, 41

Snowden, S. L., McCammon, D., Burrows, D. N., Mendenhall, J. A. 1994, ApJ, 424, 714

Soker, N. & Sarazin, C. L., 1990, ApJ, 348, 73

Taylor, G. B., Allen, S. W. & Fabian, A. C., 1999, in Böhringer *et al., op cit*, p. 77

Taylor, G. B., Govoni, F., Allen, S. A. & Fabian, A. C., 2001, MNRAS, in press

Taylor, G. B. & Perley, R. A., 1993, ApJ, 416, 554

Taylor, G. B., Perley, R. A., Inoue, M., Kato, T., Tabara, H. & Aizu, K., 1990, ApJ, 360, 41

Taylor, G. G., Barton, E. J. & Ge, J.-P., 1994, AJ, 107, 1942

Thomas, P. A., Fabian, A. C. & Nulsen, P. E. H., 1987, MNRAS, 228, 973

Tonry, J. L., 1985, ApJ, 291, 45

Turland, B. D., 1975, MNRAS, 170, 281

Völk, H. J., & Atoyan, A. M., 1999, *Astropart. Phys.*, 11, 73
Westbury, C. F. & Henriksen, R. N., 1992, *ApJ*, 388, 64
White, D. A., Jones, C. & Forman, W., 1997, *MNRAS*, 292, 419
Zhou, J.-H., Sumi, D. M., Burns, J. O. & Duric, N., 1993, *ApJ*, 416, 51

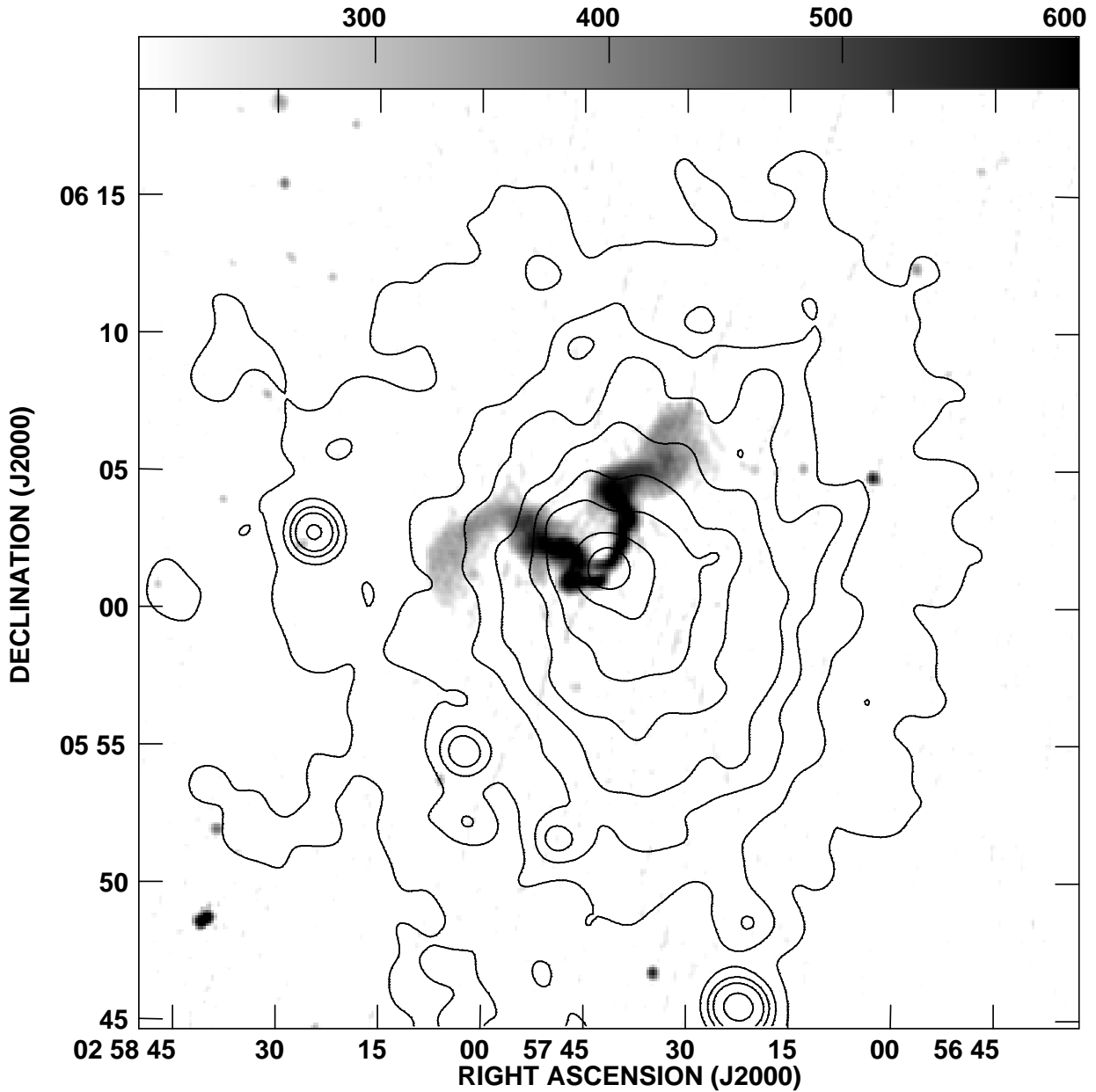


Fig. 1.— Abell 400 and 3C75. The contours show the X-ray emission from A400, observed with the ROSAT PSPC, convolved to 80 asec ~ 35 kpc resolution. The grey scale shows a 327 MHz VLA image of 3C75. The image is 900 kpc on a side.

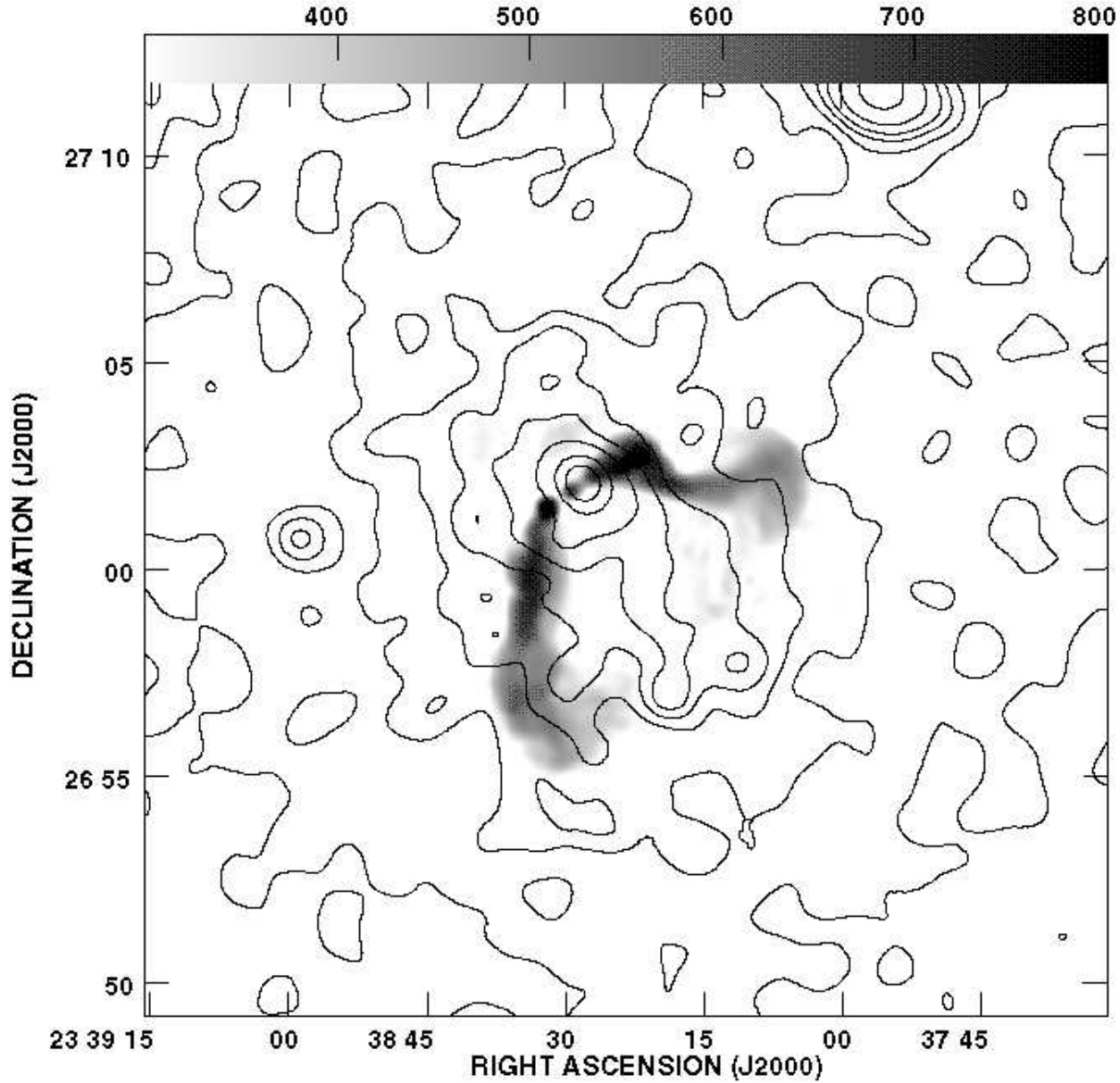


Fig. 2.— Abell 2634 and 3C465. The contours show the X-ray emission from A2634, observed with the ROSAT PSPC, convolved to 60 asec \sim 35 kpc resolution. The grey scale shows a 327 MHz VLA image of 3C465. The image is 900 kpc on a side.

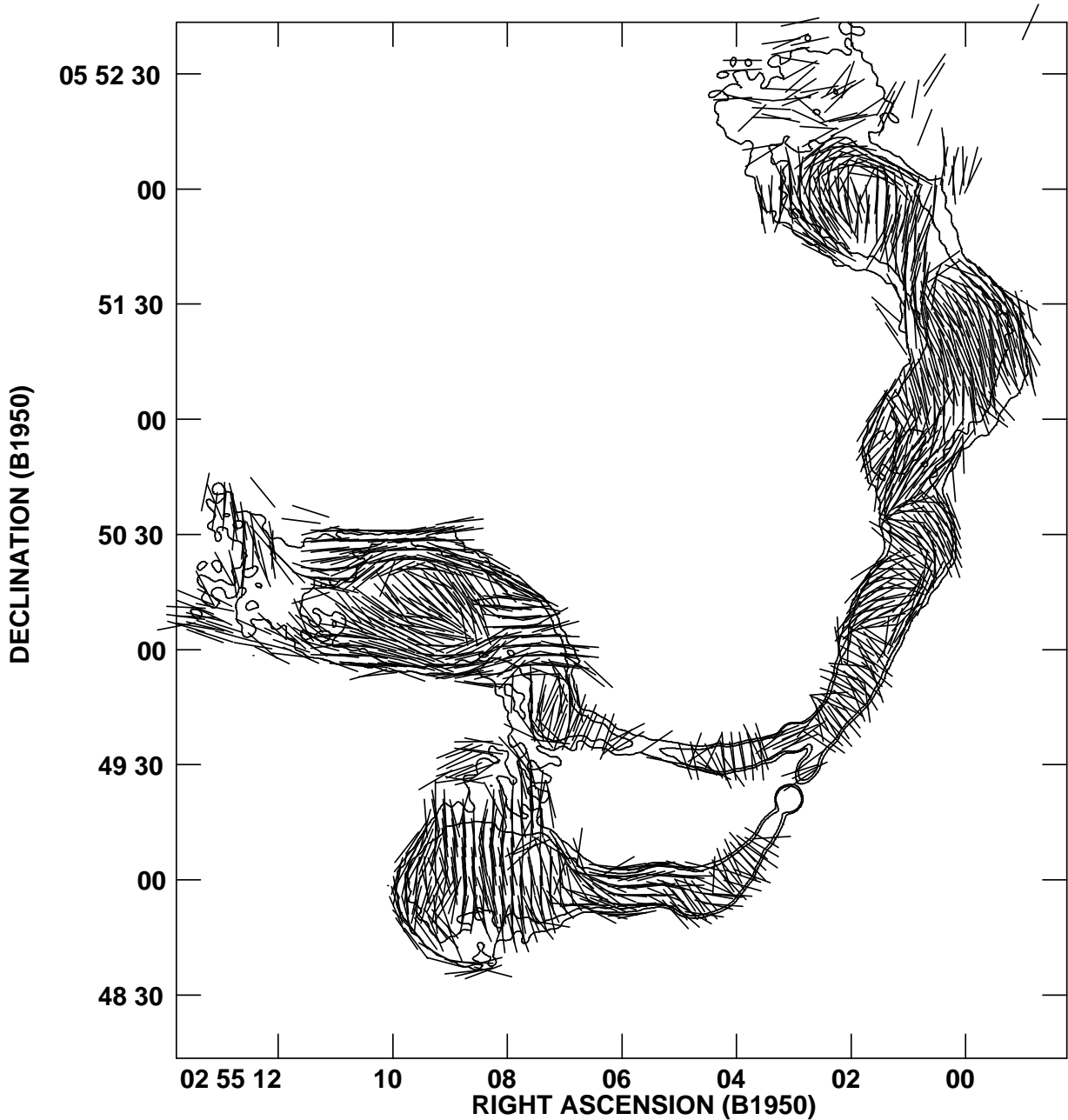


Fig. 3.— Magnetic field vectors, projected on the sky, for 3C75. Faraday rotation has been accounted for, so that the intrinsic field direction can be determined. All vectors have the same length; no attempt has been made to display the fractional polarization. The contours refer to the 5 GHz radio image.

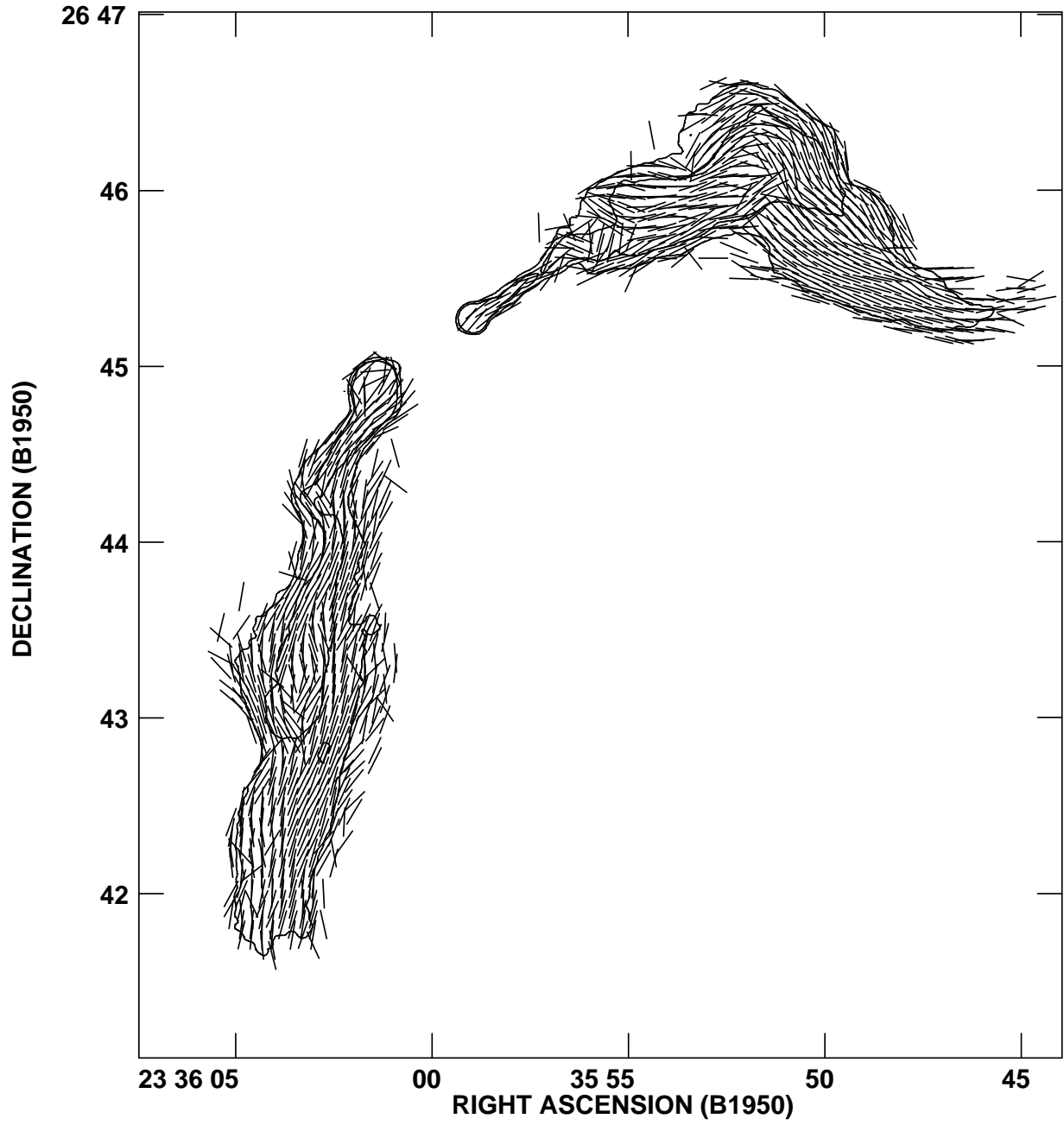


Fig. 4.— Magnetic field vectors, projected on the sky, for 3C465. Faraday rotation has been accounted for, so that the intrinsic field direction can be determined. All vectors have the same length; no attempt has been made to display the fractional polarization. The contours refer to the 5 GHz radio image.

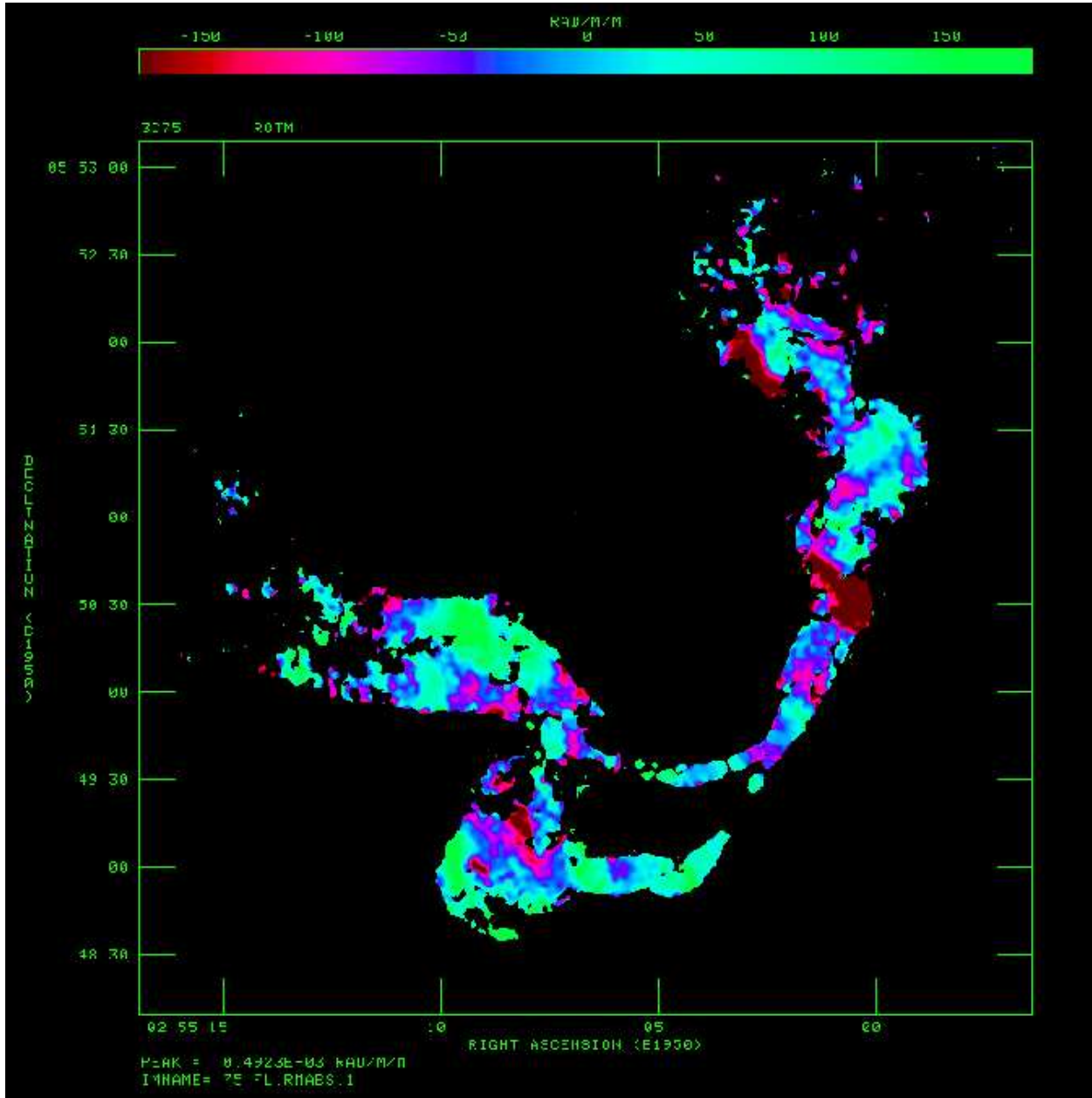


Fig. 5.— Rotation measure distribution in Abell 400. The colors are chosen to distinguish positive (green and light blue) and negative (red and dark blue) values. One arcmin is 26.5 kpc.

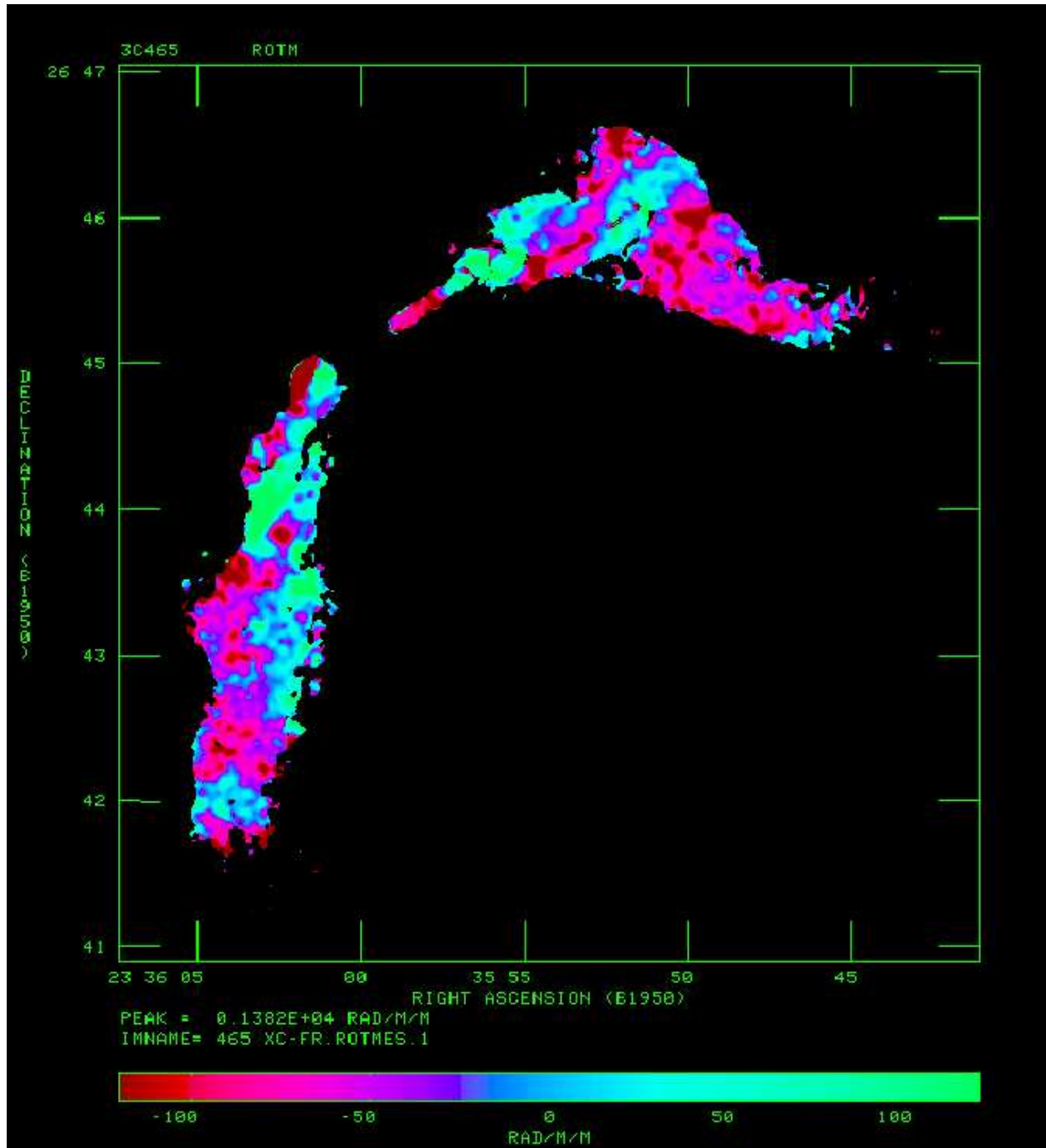


Fig. 6.— Rotation measure distribution in Abell 2634. The colors are chosen to distinguish positive (green and light blue) and negative (red and light blue) values. One arcmin is 35.2 kpc.

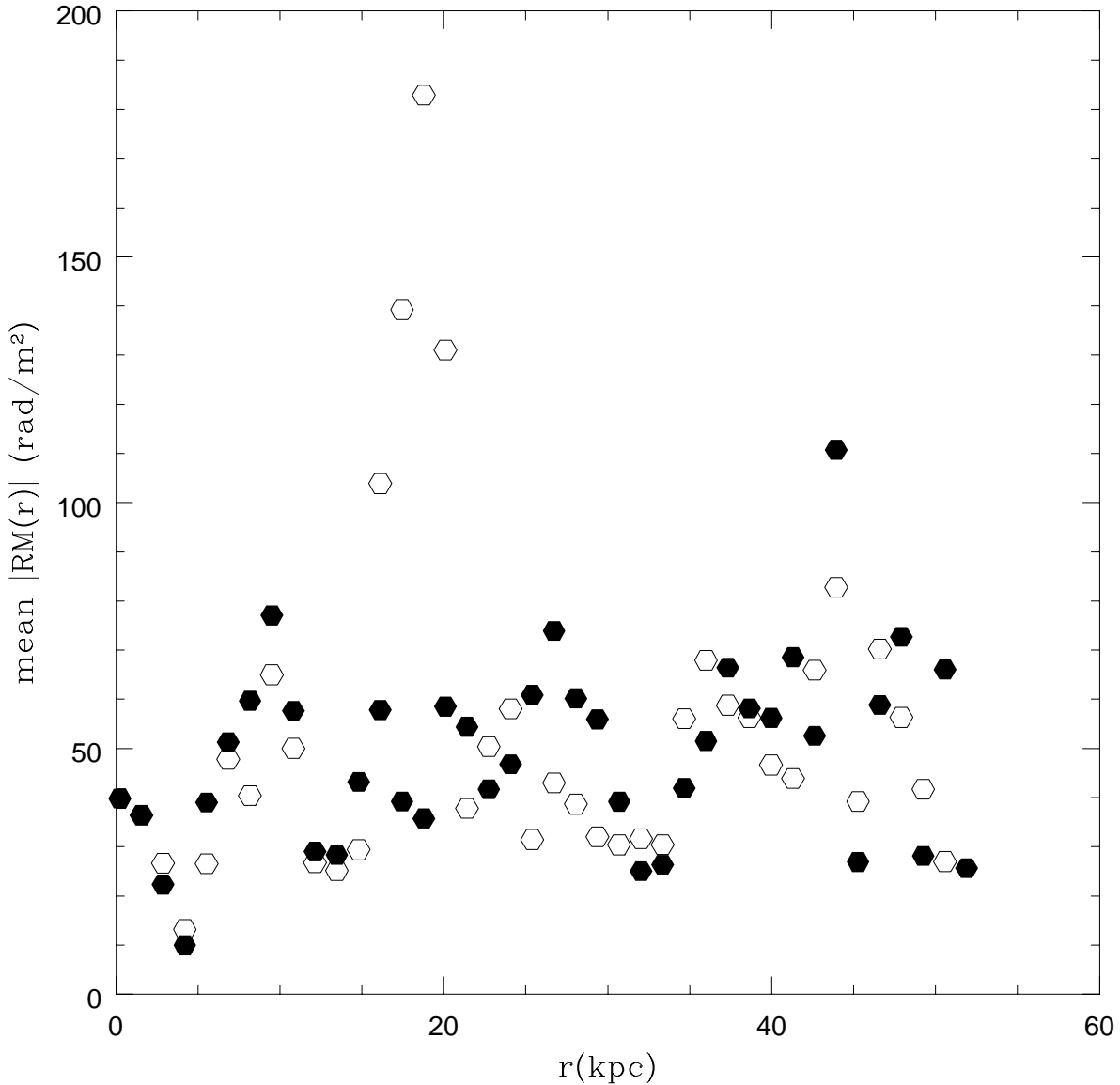


Fig. 7.— Absolute value of the rotation measure in Abell 400, as a function of distance. The points are means within circular rings centered on the radio core. The east tail is shown as solid points, and the west tail as open circles. The strongly negative RM patch on the west tail is apparent at ~ 150 rad/m².

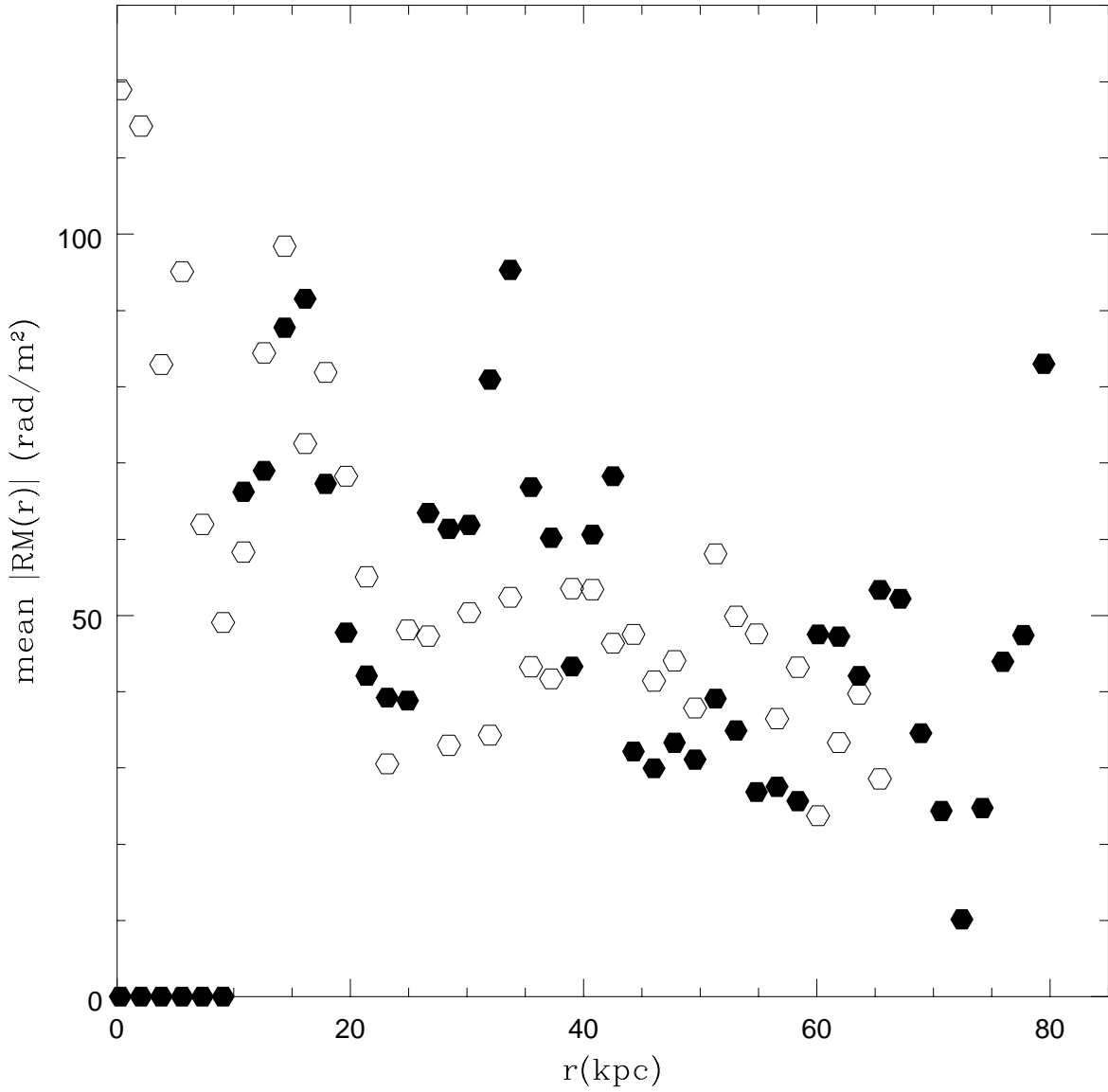


Fig. 8.— Absolute value of the rotation measure in Abell 2634, as a function of distance. The points are means within circular rings centered on the radio core. The east tail is shown as solid points, and the west tail as open circles. Note the decay of $|\text{RM}|$ with distance in this cluster.

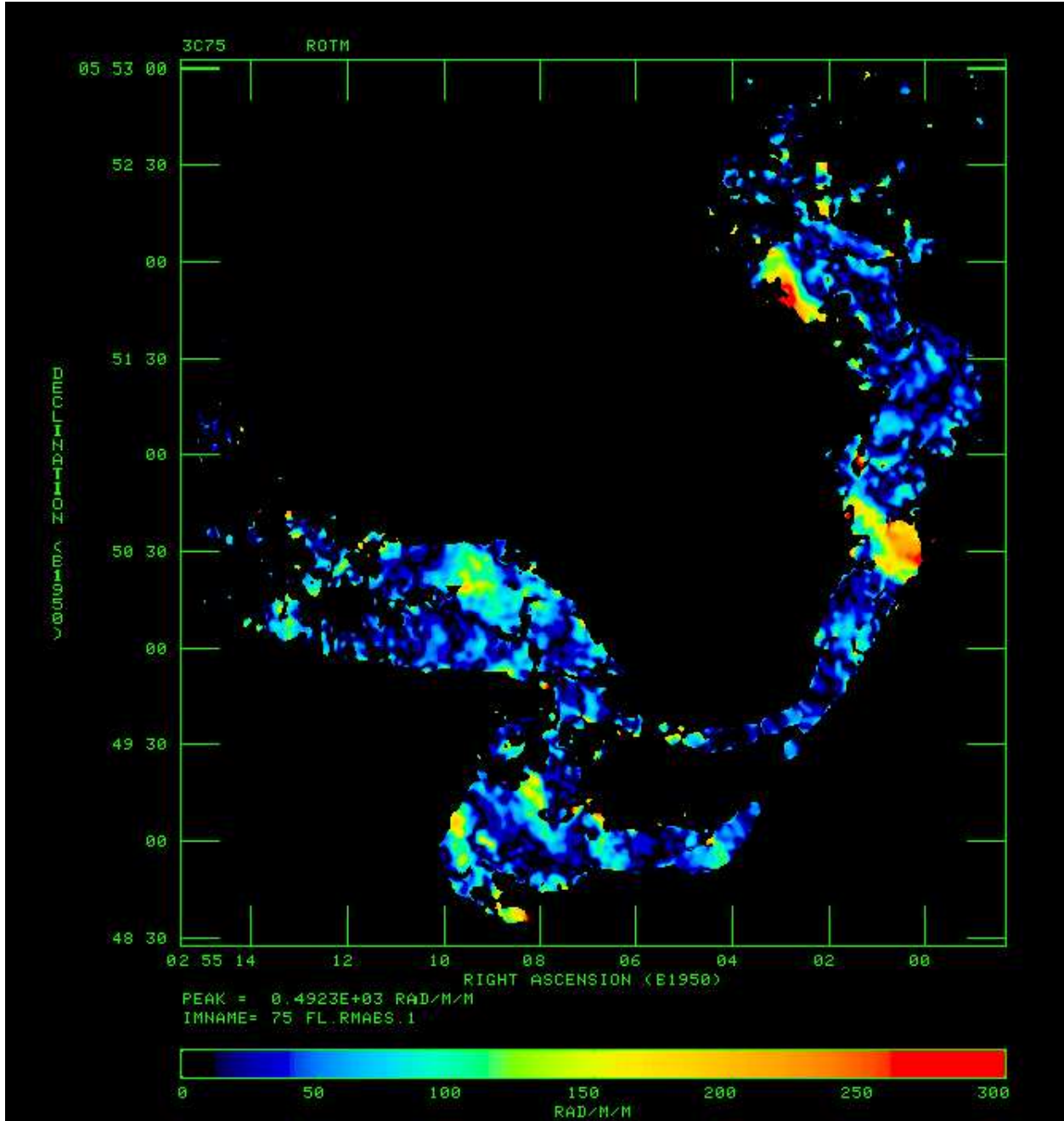


Fig. 9.— Absolute value of the RM in 3C75. The colors are chosen to highlight extreme values of the RM: the bright yellow patches on the west tail reach -300 rad/m 2 (northerly patch) and -200 rad/m 2 (southerly patch).

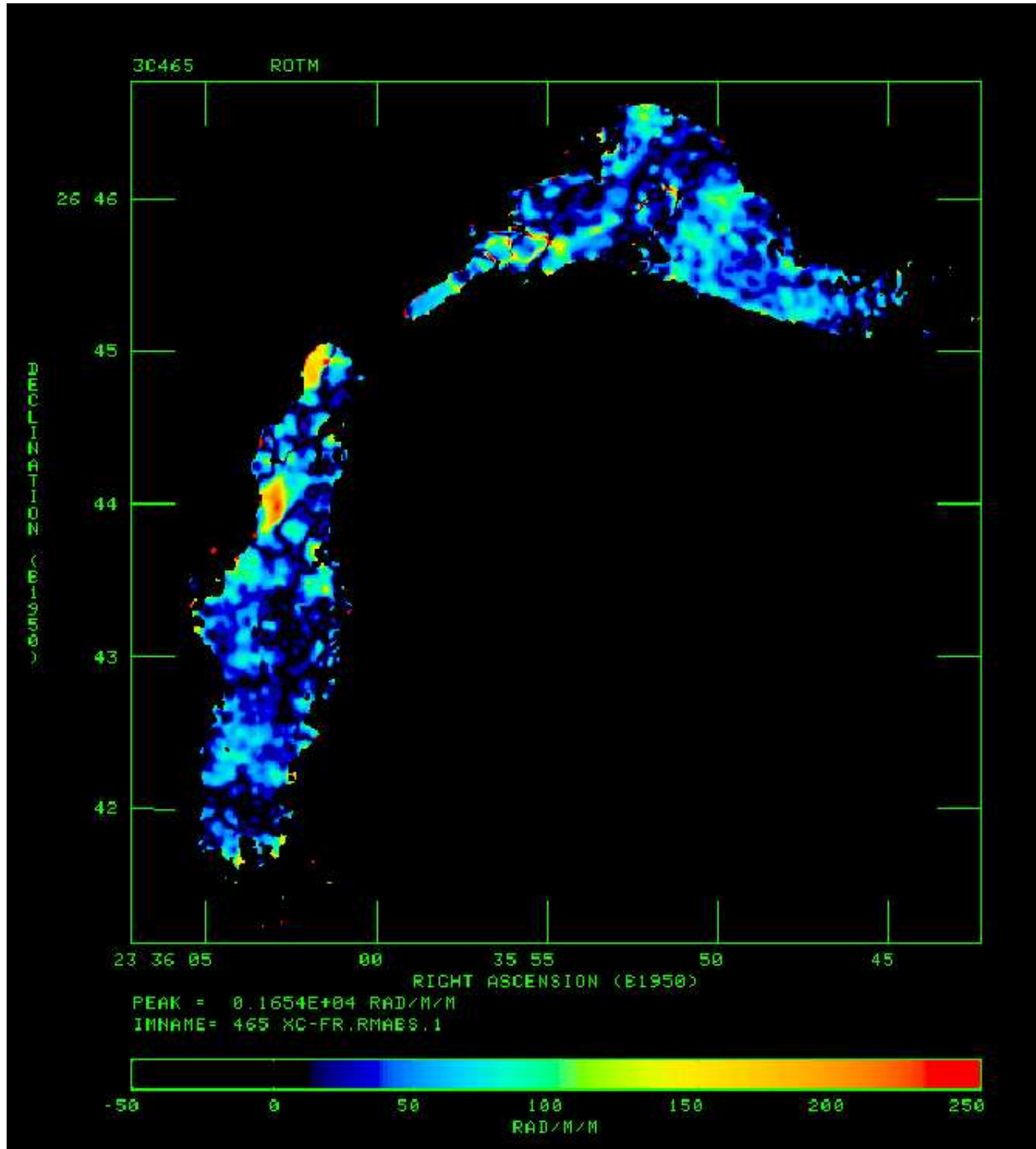


Fig. 10.— Absolute value of the RM in 3C75. The colors are chosen to highlight extreme values of the RM: the bright yellow patches on the east tail reach -200 rad/m² (northerly patch) and +250 rad/m² (southerly patch).

Table 1. X-ray Emitting ICM in A400 and A2634

Abell 400			Abell 2634		
\sqrt{ab}^1 (kpc)	n (cm $^{-3}$)	T (keV)	\sqrt{ab}^1 (kpc)	n (cm $^{-3}$)	T (keV)
10	6.5×10^{-3}	1.0
25	3.0×10^{-3}	1.0	25	4.7×10^{-3}	1.0
50	2.1×10^{-3}	1.5	50	1.6×10^{-3}	1.0
90	1.4×10^{-3}	1.5	80	1.1×10^{-3}	2.2
175	8.4×10^{-4}	1.4	150	8.3×10^{-4}	3.0
330	3.5×10^{-4}	1.4	290	4.8×10^{-4}	2.4
530	1.5×10^{-4}	1.6	505	2.7×10^{-4}	2.4
750	1.0×10^{-4}	1.6	780	6.2×10^{-4}	1.4

$^1\sqrt{ab}$ is the geometric mean of the major and minor semi-axes, based on ellipse fits to the surface brightness.

Table 2. Magnetic Field Models in A400 and A2634

Model	Abell 400			Abell 2634		
	L_{RM}^1 (kpc)	$\langle B_{\parallel} \rangle$ (μG)	p_B/p_g	L_{RM}^1 (kpc)	$\langle B_{\parallel} \rangle$ (μG)	p_B/p_g
thin skin	1.2	25	14.	0.7	96	420.
single feature	10.	2.9	.71	20.	3.5	.52
filled core	$10\sqrt{10}$.93	.071	$20\sqrt{10}$	1.1	.055
extrema	4.4	6.7	1.1	4.1	16.	12.

$^1L_{\text{RM}}$ is the “typical” order scale of the RM structure, used in equation (2).

2 Filled core assumes 10 filaments, the maximum possible, along the line of sight within cluster core.

3 All models assume $n = .0026$ cm $^{-3}$, $T = 1.5$ keV for A400; $n = .0011$ cm $^{-3}$, $T = 1.5$ keV for A2634.

Table 3. Cluster Core ICM and Magnetic Fields

Source	D kpc	\dot{M} M_{\odot}/yr	RM rad/m ²	L_{RM} kpc	$\langle n \rangle$ cm ⁻³	T_x keV	$\langle B_{\parallel} \rangle^2$ μG	p_B/p_g^2
A 400	100	~ 0	50	10	.0021	1.5	2.9	.19
A 1795	7	400	1500	3	.064	5.1	9.7	.021
A 2029	8	370	1500	3	.038	7.8	16	.064
A 2052	10	90	400	2	.022	2.4	11	0.17
A 2199	30	150	750	3	.020	2	15	.44
A 2634	140	~ 0	65	20	.0011	1.5	3.5	.55
A 3526	3	30	500	1	0.10	3	6.5	.01
A 4059	10	120	2000	3	.016	3.5	51	3.5
3C129	16	~ 0	200	3	.0043	6	19	1.0
Cyg A	70	200	1500	10	.014	4	15	0.22
Hydra A	50	600	2000	5	.0063	1.8	78	40
Virgo A	3	10	2000	0.85	.082	1.1	35	1.0

¹The spatial extent over which the RM has been measured; may be smaller than the physical extent of the RS.

²All calculations assume one magnetic filament, with width L_{RM} , accounts for the observed RM. If N filaments contribute, $\langle B_{\parallel} \rangle$ is reduced by \sqrt{N} , and p_b/p_g should be reduced by N .

Table 4. Cluster Core Radio Sources and Environment

Source	D kpc	B_{mp} μG	$\langle B_{\parallel} \rangle$ μG	P_{rad} erg/s	p_g dyn/cm ²	τ_E Myr
A 400	100	7	2.9	7.4×10^{41}	5.1×10^{-12}	240
A 1795	7	50	9.7	1.6×10^{41}	5.2×10^{-10}	39
A 2029	8	22	16	3.1×10^{42}	4.7×10^{-10}	2.7
A 2052	10	25	11	1.6×10^{42}	9.0×10^{-11}	1.8
A 2199	30	15	15	1.9×10^{42}	6.4×10^{-11}	32
A 2634	140	6	3.5	1.1×10^{42}	2.6×10^{-12}	230
A 3526 ¹	3	...	6.5	7.4×10^{40}	4.8×10^{-10}	13
A 4059	10	40	51	2.0×10^{41}	9.0×10^{-11}	16
3C129 ¹	16	...	19	1.5×10^{41}	4.1×10^{-11}	82
Cyg A	70	25	15	2.6×10^{44}	9.0×10^{-11}	4.1
Hydra A	50	27	18	1.8×10^{43}	1.8×10^{-11}	4.4
Virgo A	3	22	35	5.4×10^{41}	1.4×10^{-10}	0.25

¹ B_{mp} data not available